The Interplay Between Aerodynamic Instability and Other Instability Mechanisms in the Hyperloop System

Mouad Ouggaâli

TU Delft

HARDT HYPERLOOP

The Interplay Between Aerodynamic Instability and Other Instability Mechanisms in the Hyperloop System

by

Student Name	Student Number
Mouad Ouggaâli	5095107

to obtain the degree of Master of Science
at the Delft University of Technology
to be defended publicly on Monday November 11, 2024

Thesis committee:

Dr. ir. K.N. van Dalen (chairman)	Dynamics of Solids and Structures - CEG
Dr. J. Paul (daily supervisor)	Dynamics of Solids and Structures - CEG
Dr. ir. A.B. Fărăgău	Dynamics of Solids and Structures - CEG
Dr. ir. O. Colomes Gene	Offshore Engineering - CEG
Sascha Lamme	Hardt Hyperloop B.V.
ir. R.J. van Leijden	Dynamics of Solids and Structures - CEG

TU Delft

HARDT HYPERLOOP

Acknowledgements

In the name of Allah, the most gracious, the most merciful.

First, I want to thank Allah for putting me in this position and for granting me the strength and knowledge to complete my thesis.

This thesis is my final report to complete the master's in Structural engineering, specialising in the applied dynamics of structures, at the Faculty of Civil Engineering and Geosciences, Delft University of Technology. My career at TU Delft has come to an end, and I can say that this journey was very interesting and not the easiest. People often say, "Time flies when you are having fun." Time was flying by, although I am not entirely sure about the "having fun" part. After all, I enjoyed working on this thesis and am deeply thankful for the people who supported me throughout these challenges.

I want to thank my parents, sister, brothers, and the rest of my family for always standing by my side. Their mental support helped me to get through my bachelor's and master's studies. I am looking forward to receiving my master's degree with them by my side and sharing this beautiful moment.

I am truly grateful to have Jithu Paul as my supervisor. From the beginning you set me on the right path, explaining the complex theories very well, which me helped speed through the problems on a high-speed train, or should I say, a Hyperloop. My interest in dynamics came from the lessons and passion of Karel van Dalen, especially during the moving load courses, which eventually led me to this position. You dedicate your time to helping us understand the dynamics, which is something I appreciate. Even with your busy schedule, you always made time for my questions. Andrei Fărăgău, you were always willing to help and explain new theories, especially when it came to the complexity of the beam dynamics. Rens van Leijden, thank you for helping me with the parametric instability section of my thesis, which turned out to be the most challenging part. I am proud of the results I achieved. Although I only had very few questions for Oriol Colomes Gene, you made the concept of aeroelastic forces more understandable and helped refine my thesis. Finally, I want to thank Sascha Lamme for showing me how things work in practice and making the engineering team at Hardt Hyperloop available for questions.

Mouad Ouggaâli
Amsterdam, November 2024

Summary

Hyperloop is a new high-speed transportation system currently in development. Utilising an electromagnetic suspension within a low-pressure tube, this approach eliminates the traditional wheel-track friction and drastically reduces the air resistance, targeting speeds up to 1000 km/h. Compared to traditional trains and aeroplanes, the Hyperloop is a more sustainable alternative as it produces no greenhouse gas emissions and uses ten times less energy than road and aviation transportation. The Hyperloop, therefore, has great potential to contribute to the goal of achieving climate neutrality by 2050.

Ensuring the stability of the Hyperloop is a critical challenge in its realisation. Multiple instability mechanisms are present in the system: (1) electromagnetic instability, (2) wave-induced instability, and (3) aeroelastic effects, such as galloping. Additionally, the imperfections in the guideway, make the Hyperloop system prone to parametric instability. This thesis primarily investigates how aeroelastic forces and parametric resonance interact with the electromagnetic and wave-induced instability mechanisms, impacting the overall stability of the Hyperloop system.

Based on the results, it can be concluded that the aeroelastic force destabilises the system, where its impact increases as the velocity rises. As the aeroelastic force continuously injects energy into the system, the unstable domain expands. Furthermore, parametric resonance, represented by ellipse-shaped indentations in the stability planes, is observed when the excitation frequency is twice the natural frequency of the system. Based on the control parameter range used for maglev trains, it is found that the stable domain is narrow, with only a small region prone to parametric resonance. Therefore, choosing the control parameters precisely is essential to prevent instability and parametric resonance.

When examining the combined effect of aeroelastic force and the irregular guideway profile, the results show that the aeroelastic force shifts the overall position of the stability boundaries but it does not affect the parametric resonance regions. Instead, the amplitude of the guideway's irregular profile influences the size of the ellipses and the stable domain. A larger amplitude leads to an expansion of the unstable domain and an increase in the size of the ellipse; therefore, it is advised to maintain a smooth guideway.

This thesis further evaluates the capabilities of analytical expressions for the simpler 1.5 degree-of-freedom (DOF) electromagnetically suspended mass system by comparing it to systems that incorporate the beam dynamics. The results show that the analytical expressions from the 1.5 DOF system cannot approximate the position of the ellipses for the more complicated systems across all velocities. However, beyond the velocities of $1.3v_{cr}$, the analytical expressions effectively approximate the ellipse size. Notably, while the position and size of the ellipse are influenced by the guideway's surface roughness amplitude, only the size of the ellipse is affected by the amplitude of the oscillations in the 1.5 DOF system. For the more complicated systems, the analytical expressions of the ellipse size relative to the amplitude provide accurate results, making the simplified system a valuable approach for estimating the ellipse size of parametric resonance in systems with beam dynamics.

Keywords: Hyperloop, Stability, Maglev, Wave-induced instability, Electromagnetic instability, Aeroelastic force, Galloping, Modulated aeroelastic force, Parametric resonance

Contents

List of Figures

List of Tables

1 Introduction

1.1. Background

By 2050, the world population is expected to grow by two billion people [33]. As a result, the transportation demand will nearly triple from 44 trillion to 122 trillion passenger kilometres [12]. This demand will lead to a rise in greenhouse gas emissions, which urgently needs to be mitigated. Expanding road infrastructure or increasing air travel will not be the most environmentally sustainable approach. Various environmentally friendly transport options are being promoted to lower the CO_2 emissions. Governments endorse alternative transportation modes such as car-sharing, trains, and cycling with a strong recommendation to limit air travel. However, these measures alone will not resolve the environmental problem, as travel for both work and leisure remains necessary. A solution is required to reduce CO_2 emissions and meet the European Union's goal to achieve climate neutrality by 2050 [5]. Moreover, as the global economy is rapidly evolving and cities are expanding, companies and people are moving out of the major cities, which increases travel time. Companies and people want to move at higher velocities to save time and money. The Hyperloop could be the solution to all these challenges.

In 2013, Elon Musk introduced the concept of the 'fifth transportation mode', named the Hyperloop. The Hyperloop is an innovative transportation system that combines elements of a train system with the high speeds of an aeroplane. Operating inside a low-pressure tube using an electromagnetic suspension (EMS), the Hyperloop aims to reach speeds up to 1000 km/h. For instance, a trip from Amsterdam to Berlin would take ninety minutes with the Hyperloop compared to almost six hours by traditional train. While the aeroplane would be fifteen minutes faster, the Hyperloop offers greater environmental benefits. It is claimed that the Hyperloop does not emit greenhouse gases and air pollution, therefore checking the box to become a climate-neutral solution. Furthermore, the Hyperloop's energy consumption is ten times lower than road or aviation transportation [8]. However, as the Hyperloop concept is still in its early stages, further research is required to address the challenges and ensure its success.

1.2. Problem Statement and Research Gap

Although the Hyperloop is still in its early development stages, there is significant interest from the research community [7]. Stakeholder interest has also grown over the years [22]. There are still uncertainties regarding aspects such as the tube diameter, whether the vehicle will float above the track or be suspended from it, the final achievable speed, the type of suspension system, and more [23, 25]. These questions show the need for further research and development to realise the Hyperloop.

Various companies worldwide are focused on the development of the Hyperloop technology, with the aim of creating a sustainable, high-speed transportation system for the future. By 2040, passengers should be able to use the Hyperloop system. However, the high velocities raise concerns about the vehicle's stability. With an air gap of only a few millimetres between the vehicle and the guideway, significant vibrations could cause the vehicle to collide with the guideway or the tube. Additionally, the continuous oscillations of the vehicles passing over the guideway could lead to fatigue, which is a critical challenge to the guideway's durability. Moreover, the comfort of passengers and cargo is another

important consideration. The Hyperloop must offer a comfortable experience for people to choose it as their transportation mode.

The interactions between the vehicle and the structure influence the vehicle's stability. The vehicle and guideway can be modelled as a moving mass on a flexible beam. Aeroelastic forces, electromagnetic effects, wave-induced mechanisms, and guideway irregularities are among the contributors that influence the vehicle's stability.

The interaction between a moving load and a flexible structure has been widely studied. Denisov et al. [4] were the first to observe that the moving object on a flexible structure can become unstable when it reaches the critical velocity. Metrikine has also explored the subject of moving load dynamics. Metrikine [21] found that lateral oscillations of moving objects become unstable when the radiation of anomalous Doppler waves is larger than the radiation of normal Doppler waves. The moving object extracts energy from the flexible structure when its velocity exceeds the minimum phase velocity of the radiated waves. Mazilu et al. analysed the influence of non-contact forces between a moving mass and an Euler-Bernoulli beam in various systems. Using models with one contact point [18] and multiple contact points [17], Mazilu et al. found the presence of limit cycles when the masses move at supercritical velocities.

Researchers have also conducted numerous studies on the behaviour of electromagnetic suspensions and their interaction with flexible structures. Several studies [10, 32, 39] have analysed the stability of an EMS using a single-degree-of-freedom for the flexible structure. Fărăgău et al. [6] analysed the interplay between the electromagnetic and wave-induced instability mechanisms. This thesis can be viewed as a continuation of that paper.

The number of studies on aerodynamics, galloping and flutter, related to moving objects remains limited. Most studies on galloping and flutter are focused on fluid mechanics. Wu et al. [36] and Liu et al. [16] investigated the stability of an electromagnetically suspended mass subjected to aeroelastic forces while moving over a rigid guideway. To the best of the authors' knowledge, Yau [40] is the only researcher that has combined the effects of electromagnetic suspensions, flexible structures and aeroelastic forces, where the flexible structure is modelled as a single-degree-of-freedom system.

Moreover, parametric instability related to moving loads has been widely studied in numerous research studies. Metrikine [20] analysed the stability of a moving mass on a periodically supported string. A notable finding was that both anomalous Doppler waves and normal Doppler waves are excited simultaneously in the periodically inhomogeneous system, regardless of the velocity. Inoue et al. [11] investigated an electromagnetic levitation system subjected to a harmonic external force.

1.3. Aim and Scope

This thesis focuses on determining the stable domain of the Hyperloop system within the plane of control parameters for the PD controller used in the electromagnetic suspension. A parametric study is conducted to analyse the influence of the various parameters on the stability boundaries. The examined parameters are the vehicle's velocity, the bending stiffness, the amplitude and wavelength of the surface roughness, and the aeroelastic force. This analysis provides an understanding of the factors affecting the Hyperloop's stability.

The first objective is to examine the stability of an infinite Euler-Bernoulli beam that is continuously supported by a viscoelastic foundation and subjected to a moving mass suspended from the beam through the electromagnetic suspension. The mass is subjected to a constant aeroelastic force. In this model, the tube is also considered as part of the guideway, therefore disregarding shell dynamics. This analysis aims to show how the constant aeroelastic force influences the stability of the system, in combination with the electromagnetic and wave-induced instability mechanisms.

The second objective is to analyse the stability of an irregular infinite Euler-Bernoulli beam that is continuously supported by a viscoelastic foundation and subjected to a moving mass suspended from the beam through the electromagnetic suspension. The irregular profile of the guideway is approximated using a cosine function. This analysis focuses on the influence of parametric resonance on the stability boundaries, and how these stability boundaries change when the amplitude and wavelength of the irregular guideway profile are varied. This system is compared to the 1.5-degree-of-freedom (DOF) electromagnetically suspended system with an oscillating base to evaluate its accuracy in approximating the behaviour of more complicated systems.

The third objective is a combination of the first and second objectives, by introducing the constant aeroelastic force into the system with the irregular guideway profile. This analysis examines how the constant aeroelastic force influences the regions of parametric resonance induced by the irregular guideway profile and the interplay between aerodynamic, electromagnetic, and wave-induced instabilities. This model is compared to the 1.5 DOF system that is subjected to a constant aeroelastic force, to evaluate whether the 1.5 DOF system can approximate the behaviour of the more complicated system.

The fourth objective is to examine the stability of an electromagnetically suspended mass with an oscillating base that is subjected to a modulated aeroelastic force. This analysis provides insights into how the parametric resonance region is influenced by the interaction between the oscillating base and the modulated aeroelastic force, assessing whether these actions suppress or amplify parametric instability.

1.4. Research Questions

The research questions answered in this study are:

1. How does the aerodynamic instability mechanism change the stability of the Hyperloop system, when initially only considering electromagnetic and wave-induced instability mechanisms?

2. How does the irregular guideway profile impact the stability of the Hyperloop system when considering the electromagnetic and wave-induced instability mechanisms?

3. How does the aerodynamic instability mechanism impact the stability of the Hyperloop system when considering the effects of an irregular guideway profile along with electromagnetic and wave-induced instability mechanisms?

4. How does a modulated aeroelastic force influence the parametric instability of a system subjected to an oscillating boundary?

5. To what extent is the electromagnetically suspended mass system with an oscillating base capable of approximating more complicated systems that include beam dynamics and an irregular guideway profile subjected to a constant aeroelastic force?

1.5. Report Outline

This thesis consists of the following chapters:

Chapter 2 provides an overview of the theoretical framework. The solution methods for the various instability mechanisms are discussed and explained.

Chapter 3 describes the system of the continuously supported Euler-Bernoulli beam with an electromagnetically suspended moving mass and constant aeroelastic force. The system is solved in the Laplace-wavenumber domain, which is also explained in this chapter.

Chapter 4 describes the irregular Euler-Bernoulli beam with continuous support under an electromagnetically suspended moving mass and constant aeroelastic force. The system is solved using a combination of the exponential harmonic balance method and Floquet's theorem, with an explanation of this method in this chapter.

Chapter 5 focuses on the electromagnetically suspended mass on an oscillating base subjected to a modulated aeroelastic force. The system is solved using Floquet's theorem, which is explained in this chapter.

Chapter 6 presents the results of the systems described in the previous chapters. The results are then discussed, highlighting the most important observations.

Chapter 7 presents the conclusions, answering the research questions.

Chapter 8 follows with the recommendations for future research.

2

Theoretical Foundation

This chapter presents the important theories used in the thesis. First, the concept of stability and instability is explained, how they can be determined and what equilibrium points are. Next, limit cycles and bifurcations are discussed. Hereafter, the primary instability mechanisms are clarified along with the equations of motion that are used in the analysis. Finally, parametric instability is described, along with an explanation of Floquet's theorem.

2.1. Stability and Instability of Two-Dimensional Linear Systems

2.1.1. Equilibrium Points

Differential equations of dynamical systems can be written in the form [14]:

$$\ddot{x} = f(x, \dot{x}, t) \quad \text{or} \quad \ddot{x} = f(x, \dot{x}) \tag{2.1}$$

Where x is the displacement, $\dot{x}$ is the velocity, $\ddot{x}$ is the acceleration and f is the applied force, which may or may not depend on time, t. These differential equations are categorised into two types [14].

- Autonomous differential equations do not have time dependence explicitly in the forcing.
- Non-autonomous or forced equations where time appears explicitly in the forcing.

A mechanical system is in equilibrium when its state remains unchanged over time. This condition is met when $\dot{x}$ and $\ddot{x}$ are zero, such solution is called a constant solution or fixed point. Non-autonomous equations usually do not have equilibrium states because of the continuous input of energy through the forcing term, although equilibrium states can still occur [14].

The constant solutions can be obtained by solving the problem [14]:

$$f(x, 0) = 0 \tag{2.2}$$

The general solution of linear autonomous plane systems is obtained by analysing the determinant of the matrix representing the linear system [14, 31]. Consider the system:

$$\dot{x} = ax + by, \quad \dot{y} = cx + dy \tag{2.3}$$

This system can be written in matrix-vector form:

$$\dot{\boldsymbol{x}} = \boldsymbol{A}\boldsymbol{x} \quad \text{with} \quad \boldsymbol{A} = \begin{bmatrix} a & b \\ c & d \end{bmatrix}, \quad \dot{\boldsymbol{x}} = \begin{bmatrix} \dot{x} \\ \dot{y} \end{bmatrix}, \quad \boldsymbol{x} = \begin{bmatrix} x \\ y \end{bmatrix} \tag{2.4}$$

The solutions of the two linear differential equations have the form [14]:

$$\boldsymbol{x(t)} = \boldsymbol{v_1} e^{\lambda_1 t}, \quad \boldsymbol{y(t)} = \boldsymbol{v_2} e^{\lambda_2 t} \tag{2.5}$$

where λ_1, λ_2 are the eigenvalues and $\boldsymbol{v_1}$, $\boldsymbol{v_2}$ are the corresponding eigenvectors. λ_1, λ_2, $\boldsymbol{v_1}$ and $\boldsymbol{v_2}$ are determined by setting the determinant of matrix $\boldsymbol{A}$ to zero, providing nonzero solutions for the variables [14].

$$[\boldsymbol{A} - \lambda \boldsymbol{I}] = det \begin{bmatrix} a - \lambda & b \\ c & d - \lambda \end{bmatrix} = 0 \tag{2.6}$$

This results in the characteristic equation:

$$\lambda^2 - p\lambda + q = 0 \tag{2.7}$$

where

$$p = a + d, \quad q = ad - bc \tag{2.8}$$

Put

$$\Delta = p^2 - 4q \tag{2.9}$$

The eigenvalues are then given by:

$$\lambda_1, \lambda_2 = \frac{1}{2}(p \pm \Delta^{1/2}) \tag{2.10}$$

The stability of equilibrium points can be categorised into different types, known as phase paths of linear autonomous plane systems, illustrated in Figure 2.1. The values for p, q and Δ determine the classification of the equilibrium point [14].

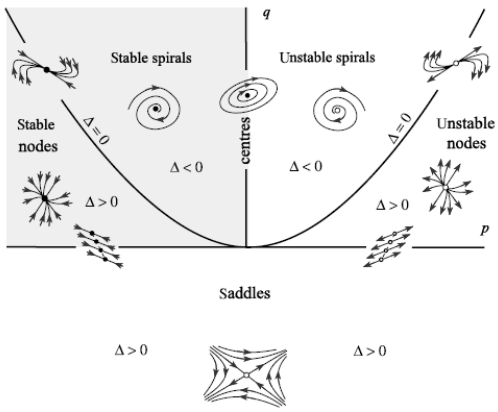

Figure 2.1: Classification of the equilibrium points

The classification of the equilibrium points can also be based on the eigenvalues. Referring to the solutions 2.5, the exponent in the solutions determines whether it grows or decays over time, which is an important criterion that is used in the stability analysis. Assuming $\lambda_1 > \lambda_2$, Table 2.1 shows the classification for equilibrium points based on the eigenvalues [14].

Equilibrium state	Eigenvalue
Saddle point	$\lambda_2 < 0 < \lambda_1$
Stable node	$0 > \lambda_1 > \lambda_2$
Unstable node	$0 < \lambda_1 < \lambda_2$
Stable spiral	$\lambda_1 = -\alpha + \beta i$, $\lambda_2 = -\alpha - \beta i$
Unstable spiral	$\lambda_1 = \alpha + \beta i$, $\lambda_2 = \alpha - \beta i$
Centre	$\lambda_1 = \beta i$, $\lambda_2 = -\beta i$

Table 2.1: Classification of the equilibrium points based on eigenvalues

Nonlinear systems

The state of nonlinear systems can be analysed similarly to linear systems by first linearising them at the equilibrium points. After applying a small perturbation to the system, the response either returns to the equilibrium point or deviates from it, revealing the stability of the equilibrium point, and making the equilibrium point an important aspect of the analysis. Linearisation can be performed using Taylor expansion. Performing Taylor's expansion at point x_0 yields [13]:

$$f(x) = f(x_0) + \frac{f'(x_0)}{1!}(x - x_0) + O(x_0^2) \tag{2.11}$$

Performing Taylor's expansion for a function of two variables, in point (x_0, y_0) gives:

$$f(x, y) = f(x_0, y_0) + \frac{f_x(x_0, y_0)}{1!}(x - x_0) + \frac{f_y(x_0, y_0)}{1!}(y - y_0) + O(x_0^2) + O(y_0^2) \tag{2.12}$$

After linearisation, the characteristic equation can be formulated to determine the eigenvalues and describe the state of the system.

N-dimensional linear system

Linear systems can have more than two dimensions. To determine the equilibrium state of an n-dimensional linear system, the Jacobian matrix, similar to that used for the two-dimensional system must be formulated. The matrix is now n x n with n eigenvalues. The same approach applies to non-linear systems with n-dimensions, which must first be linearised at the equilibrium point [14].

2.1.2. Limit Cycle

Limit cycles are closed isolated paths, meaning that there are no other closed paths near the limit cycle. There are three types of limit cycles.

1. **Stable limit cycles**: When a system is perturbed from its regular oscillatory state, it returns to the limit cycle. This indicates stability for perturbations applied on either side of the limit cycle.
2. **Unstable limit cycles**: When perturbed, the trajectories repel away from the limit cycle on both sides, indicating instability.
3. **Half-stable limit cycle**: The system returns to the limit cycle on one side and repels away on the other side when perturbed.

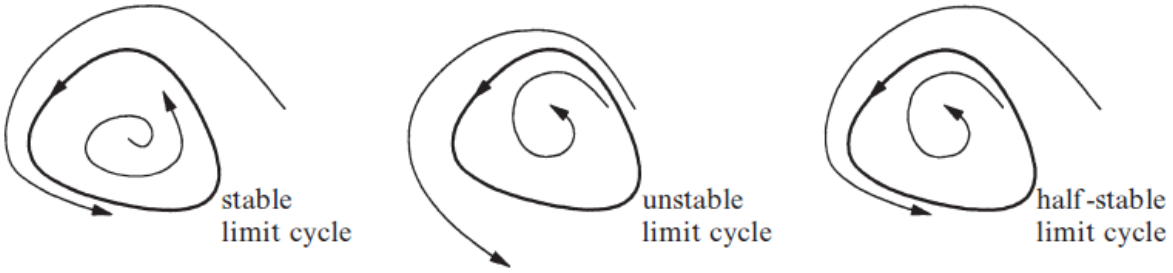

Figure 2.2: Limit cycles

Limit cycles are phenomena where a system oscillates in the absence of an external periodic forcing, occurring only in nonlinear systems. While linear systems can also have closed paths, these paths are not isolated. Therefore, a closed orbit $x(t)$ in a linear system can be surrounded by multiplications of that closed orbit, $cx(t)$ by any constant $c \neq 0$. In linear systems, the initial conditions determine the amplitude of the oscillations. For limit cycles, however, the oscillations are determined by the characteristics of the system, making them independent of the initial conditions. [31].

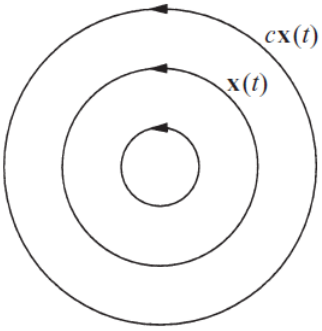

Figure 2.3: Higher order of the closed orbits for linear systems

2.1.3. Bifurcations

The stability of systems can change when the control parameters are changed. The transition from stability to instability happens when the real part of one of the eigenvalues becomes positive, leading to a qualitative change known as bifurcations. Several bifurcations exist, for example saddle-node bifurcation, transcritical bifurcation, pitchfork bifurcation, homoclinic bifurcation, hetroclinic bifurcation and Hopf bifurcation. The properties of the Hopf bifurcation are highlighted in this section [31].

Hopf bifurcations can occur for systems with two or more dimensions. There are two types of Hopf bifurcations: supercritical Hopf bifurcations and subcritical Hopf bifurcations [31].

Consider a system that depends on the control parameter μ. For small values of μ, the system shows damped oscillations. As μ increases, it can influence the system's stability. When μ exceeds a critical value μ_c, the equilibrium state loses stability because the real part of an eigenvalue has become positive. Figure 2.4 illustrates the formation of limit cycles around the previously stable steady state. This phenomenon is known as a supercritical Hopf bifurcation [31].

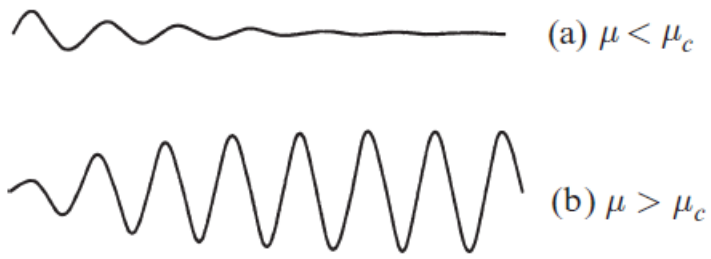

Figure 2.4: Amplitude variation in a system undergoing a supercritical Hopf bifurcation

Supercritical Hopf bifurcation can also be visualised using a phase portrait. Consider the following system in polar coordinates:

$$\dot{r} = r(\mu - r^2), \quad \dot{\theta} = -1 \tag{2.13}$$

Figure 2.5 shows that when $\mu \leq 0$, the origin is a stable spiral. However, when $\mu > 0$, the origin becomes an unstable spiral surrounded by a limit cycle [14].

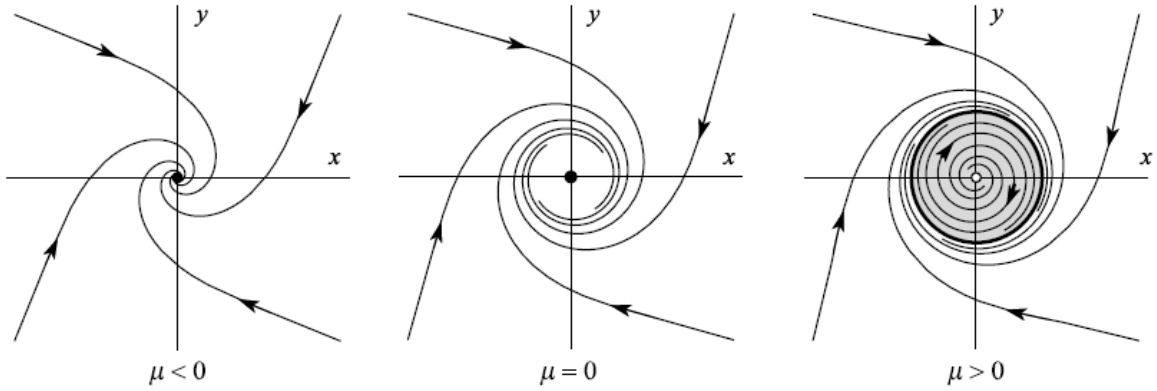

Figure 2.5: Development of a limit cycle in a supercritical Hopf bifurcation

In contrast to the supercritical Hopf bifurcation, the changes of the subcritical Hopf bifurcation are more unexpected and can result in more dangerous situations in engineering applications. After the subcritical Hopf bifurcation, the trajectories may shift to a distant attractor, which could be a fixed point, another limit cycle, infinity, or — in systems with three or more dimensions — a chaotic attractor. To illustrate the occurrence of a subcritical Hopf bifurcation, consider the following two-dimensional system where μ is the control parameter [31]:

$$\dot{r} = \mu r + r^3 - r^5 \tag{2.14}$$

$$\dot{\theta} = \omega + br^3 \tag{2.15}$$

The phase portraits show that for $\mu \leq 0$, two attractors are present: a stable fixed point and a stable limit cycle, with an unstable limit cycle in between them. The position of the unstable limit cycle shifts as μ changes. As μ increases, the amplitude of the unstable limit cycle decreases until the cycle encircles the stable fixed point at the origin. At μ = 0, a subcritical Hopf bifurcation occurs, where the

amplitude of the unstable limit cycle has reduced to zero, surrounding the origin. As a result, the limit cycle becomes the only attractor, as illustrated in Figure 2.6 [31].

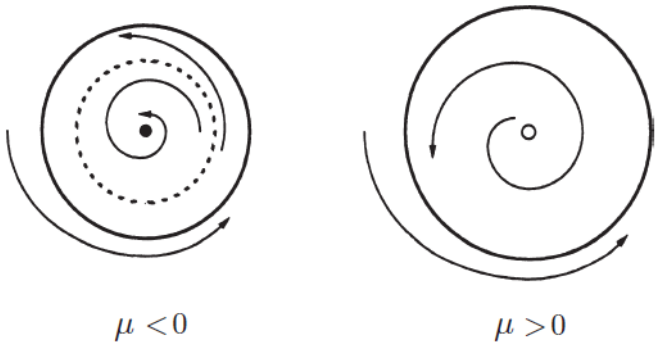

Figure 2.6: Transition of a subcritical Hopf bifurcation

2.2. Harmonic Balance Method

Nonlinear systems are complicated to solve analytically. To address this challenge, nonlinear approximation theories can be used. Harmonic balance is a powerful method to approximate a periodic solution of nonlinear systems by assuming that the solution takes the form:

$$x(t) = a_0 + \sum_{k=1}^{k} (a_k cos(k\omega t) + b_k sin(k\omega t)) \tag{2.16}$$

The objective is to determine the parameters a_0, a_k, b_k and ω. For example, take the general equation:

$$\ddot{x} + \epsilon h(x, \dot{x}) + x = 0 \tag{2.17}$$

The solution for $x(t)$ is looked for in the form $acos(\omega t)$, so $h(x, \dot{x})$ can be expressed as a Fourier series.

$$h(x, \dot{x}) \approx h(acos(\omega t), -a\omega sin(\omega t)) = A_1(a)cos(\omega t) + B_1(a)sin(\omega t) + \text{higher harmonics} \tag{2.18}$$

where

$$A_1(a) = \frac{\omega}{\pi} \int_0^{2\pi/\omega} h(acos(\omega t), -a\omega sin(\omega t))cos(\omega t)\, dt$$
$$B_1(a) = \frac{\omega}{\pi} \int_0^{2\pi/\omega} h(acos(\omega t), -a\omega sin(\omega t))sin(\omega t)\, dt$$

The equation becomes:

$$(1 - \omega^2)acos(\omega t) + \epsilon A_1(a)cos(\omega t) + \epsilon B_1(a)sin(\omega t) + \text{higher harmonics} = 0 \tag{2.19}$$

The equation is valid for all t only if

$$(1-\omega^2)a + \epsilon A_1(a) = 0 \quad \text{and} \quad B_1(a) = 0 \tag{2.20}$$

$A_1(a)$ and $B_1(a)$ are represented by the Fourier series. The accuracy of the solutions depends on the number of harmonics, with higher harmonics providing a more accurate solution to the nonlinear system [14].

The harmonic balance method can also be applied using the exponential form [15]. The steps remain the same as those used with the trigonometric functions. The only difference is that the approximated periodic solution is now expressed as:

$$x(t) = a_0 + \sum_{k=1}^{k} (a_k \exp(ik\omega t) + b_k \exp(-ik\omega t)) \tag{2.21}$$

2.3. The Instability Mechanisms

2.3.1. Electromagnetic Instability

Hardt Hyperloop uses an EMS that relies on attraction towards the track [8]. The EMS generates a nonlinear force, connecting the vehicle to the guideway. The controller used by Hardt is not the same as the one applied in this thesis. To understand the system's fundamentals, a simplified PD controller is used in the analysis. The governing equations for the electromagnetic force are described in [36].

$$F_{EM}(t) = C\frac{I^2(t)}{z^2(t)} \tag{2.22}$$

$$\dot{I}(t) + \frac{z(t)}{2C}\left(R - 2C\frac{\dot{z}(t)}{z^2(t)}\right)I(t) = \frac{z(t)}{2C}U(t) \tag{2.23}$$

$$U(t) = U_{ss} + K_p(z(t) - z_{ss}) + K_d\dot{z}(t) \tag{2.24}$$

$$C = \frac{\mu N^2 A_m}{4} \tag{2.25}$$

The EMS uses a PD controller to maintain the vehicle at a specified distance from the track, denoted as z_{ss}, which is set to 0.015 m by Hardt Hyperloop. PD controllers use both position and velocity feedback, represented by the variables K_p and K_d, respectively. K_p corresponds to the proportional gain, controlling the error at time t and can be interpreted as the coefficient that controls the present state of the system. K_d is proportional to the derivative of the error, controlling the rate of change of the error, influencing the future state of the system [1].

Furthermore, the nonlinear electromagnetic force, $F_{EM}(t)$, is a function of the current intensity $I(t)$ and the position of the vehicle $z(t)$. C is a constant that depends on the magnetic permeability in vacuum μ, the number of coils N, and the pole area of the electromagnet A_m. $U(t)$ represents the voltage applied to the system, which depends on the voltage required to maintain the vehicle at the desired distance from the guideway, noted as U_{ss}. Equation 2.24 shows that the PD controller is applied to the voltage.

2.3.2. Wave-induced Instability

Wave-induced instability is the phenomenon where waves are generated in the beam by a moving object, causing vibrations in both the beam and the moving object itself. Wolfert has analysed the effect of moving point loads in depth [35]. Using the frequency-wavenumber relation and the kinematic invariant, valuable insights can be gained regarding the behaviour of waves in one-dimensional elements. For an Euler-Bernoulli beam supported by a continuous Winkler foundation and subjected to a moving point load, the governing equation can be written as:

$$\rho A\ddot{w}(x,t) + EIw''''(x,t) + k_b w(x,t) = -P\delta(x - vt) \tag{2.26}$$

P is the magnitude of the force. $w(x,t)$ is the displacement of the beam as a function of position x and time t. k_b is the stiffness of the Winkler foundation, ρA is the mass per unit length of the beam, and EI is the bending stiffness. The Dirac delta function, $\delta(x - vt)$, marks the location of point load P, at $x = vt$.

The dispersion curve and kinematic invariant are derived by rewriting the equation of motion into the frequency-wavenumber domain. This transformation is obtained by applying the Fourier transform with respect to both position x and time t. This results in the dispersion curve and kinematic invariant:

$$k^4 - \frac{\rho A}{EI}\omega^2 + \frac{k_b}{EI} = 0 \quad \text{and} \quad \omega = kv \tag{2.27}$$

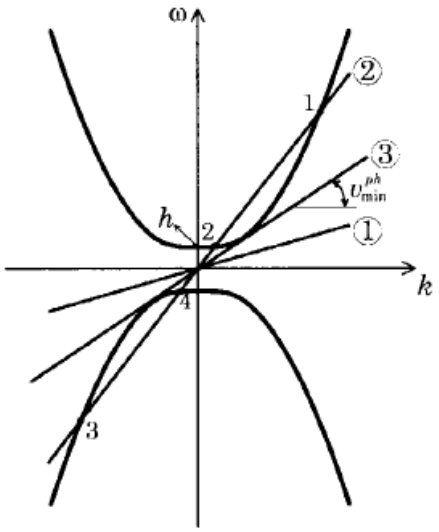

Figure 2.7: Dispersion graph with kinematic invariants

In Figure 2.7, three kinematic invariants are illustrated, each corresponding to different velocities of the moving load. The first kinematic invariant has a subcritical velocity, where the velocity of the load is lower than the critical velocity $(v < v_{cr})$. In this report, v_{cr} refers to the velocity at which the moving vehicle becomes supercritical. The critical velocity is expressed as:

$$v_{cr} = \frac{\sqrt[4]{\frac{k_b}{4EI}}}{\sqrt{\frac{\rho A}{4EI}}} \tag{2.28}$$

At subcritical velocities, the dispersion graph and kinematic invariant do not intersect, meaning there are no propagating waves in the beam. Only localised waves, also known as evanescent waves, are present around the point load. No significant energy is transferred into the beam through propagating waves. The evanescent waves decay exponentially but travel along with the point load [35].

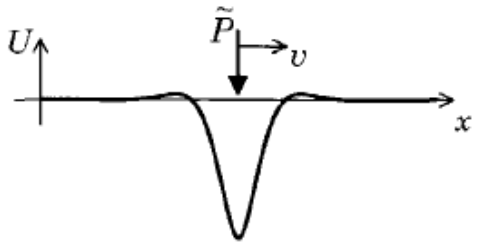

Figure 2.8: Steady-state solution at subcritical velocities

The second kinematic invariant corresponds to the supercritical case, where the velocity of the load exceeds the critical velocity $(v > v_{cr})$. In this case, the kinematic invariant intersects the dispersion graph four times, indicating that waves propagate both in front of and behind the moving load. Waves propagate in front of the moving load when the group velocity of the waves is higher than the load velocity. Waves propagate behind a moving load when the group velocity is lower than the load velocity. The group velocity of the waves is the angle between the dispersion curve and the kinematic invariant at the intersection point [35].

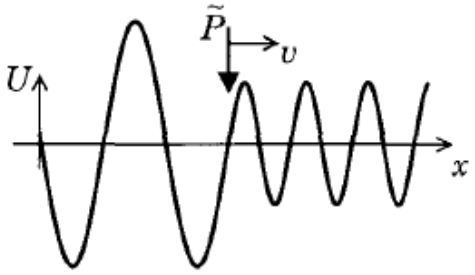

Figure 2.9: Steady-state solution at supercritical velocities

The wave propagation at supercritical velocities shows a significant difference from the subcritical case, where only evanescent waves were present. At supercritical velocities, the moving load generates a more complex wave pattern with both leading and trailing waves, indicating a higher level of interaction between the moving load and the beam.

When the load velocity equals the critical velocity $(v = v_{cr})$, the kinematic invariant becomes tangent to the dispersion graph. In this case, resonance occurs, where the frequency of the generated waves matches the beam's natural frequency. As a result, energy is continuously transferred to the beam, causing the response of the beam to grow unbounded. Therefore, a steady-state solution does not exist [35].

To this point, the focus has been on oscillations in the Euler-Bernoulli beam caused by the moving load. However, the oscillations in the Euler-Bernoulli beam can also influence the oscillations of the moving object. Metrikine [21] found that the oscillations of the moving object depend on the waves radiated by the beam. The types of waves that can be radiated are either normal Doppler waves or anomalous Doppler waves. The radiation of normal Doppler waves reduces the energy associated with the lateral oscillation of the moving object because of the energy dissipation in the beam, resulting in more stable oscillations of the moving object. In contrast, anomalous Doppler waves increase the energy of the lateral oscillation. The continuous input of energy into the moving object has a destabilising effect, potentially leading to instability.

2.3.3. Galloping

Galloping is an aerodynamic instability mechanism that commonly occurs in bluff bodies, where the structure oscillates perpendicular to the wind direction. When a structure moves vertically with velocity v and is subjected to a horizontal wind with velocity V, it experiences the wind at an angle $tan^{-1}(\frac{v}{V})$, as illustrated in Figure 2.10. In the case of the Hyperloop, the wind velocity is assumed to be equal to the velocity of the vehicle, meaning that influences from outside the tube are neglected. When galloping occurs, the load can maintain itself through the motion, but this depends on the shape of the structure, the wind velocity and the damping characteristics [3, 30].

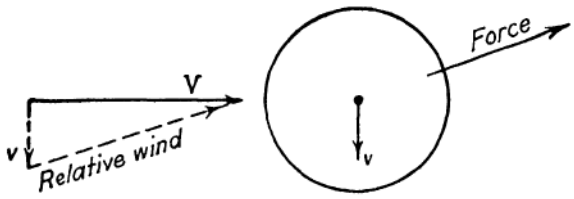

Figure 2.10: Horizontal wind and a circular cross-section moving downwards

A structure subjected to aeroelastic forces experiences two primary wind components. The first component is the wind factor parallel to the wind direction, known as drag, which resists the horizontal motion of the structure. The second component is the wind factor perpendicular to the wind direction, known as lift, which can either stabilise or destabilise the structure, depending on the interaction between the wind and the shape of the structure. The expressions for the drag and lift force are as follows:

$$F_L = \frac{1}{2}\rho_{air} A_v v^2 C_L \tag{2.29}$$

$$F_D = \frac{1}{2}\rho_{air} A_v v^2 C_D \tag{2.30}$$

C_L refers to the lift coefficient, C_D is the drag coefficient, A_v is the frontal area of the structure, ρ_{air} is the density of air and v is the wind velocity.

The vertical force component is required for the calculations, which is the resultant of the drag force and the lift force, depending on the angle of attack α [30].

$$F_z = F_L(\alpha)cos(\alpha) + F_D(\alpha)sin(\alpha) \tag{2.31}$$

For small values of α, the following approximation is made:

$$F_z = \frac{1}{2}\rho_{air} A_v v^2 \left(\frac{dC_z}{d\alpha}\right)_0 \tag{2.32}$$

The sign of $\left(\frac{dC_z}{d\alpha}\right)_0$ determines the damping characteristics of the system. If $\left(\frac{dC_z}{d\alpha}\right)_0 > 0$, it indicates that the aeroelastic force and motion are in opposite directions, reducing the amplitude of the oscillation and stabilising the system. If $\left(\frac{dC_z}{d\alpha}\right)_0 < 0$, the force and motion are in the same direction. This leads to an amplification of the oscillations, making the system unstable. In this thesis, the aeroelastic force is assumed to be destabilising [30].

$$\left(\frac{dC_z}{d\alpha}\right)_0 > 0 \quad \text{(Positive damping)} \tag{2.33}$$

$$\left(\frac{dC_z}{d\alpha}\right)_0 < 0 \quad \text{(Negative damping)} \tag{2.34}$$

2.4. Parametric Instability

Perfect constructions do not exist in reality. Guideways contain imperfections due to factors such as the foundation or surface roughness. These imperfections can sometimes be present in a periodic pattern, introducing time-dependent variations to the system parameters. These small periodic variations can generate a significant response or even resonance, also known as parametric resonance [20, 24].

Parametric resonance poses a more dangerous risk compared to classical resonance. In classical resonance, the amplitude of the oscillations increases linearly. However, with parametric resonance, the amplitude grows exponentially, leading to a rapid and potentially catastrophic response.

An important discussion is the role of damping on the two types of resonances. In classical resonance, damping can significantly reduce the oscillation amplitude, stabilising the system. In contrast, damping does not eliminate parametric resonance but it shifts the conditions under which it occurs. Metrikine [20] discovered that an increase in the damping can actually widen the main instability zone.

2.4.1. Floquet Theory

Linear ordinary differential equations with periodic parameters can be analysed using Floquet's theorem. To determine the stability boundary for a multi-degree-of-freedom system, the Floquet eigenvalues are evaluated. The stability of the system depends on the real part of one of the Floquet eigenvalues. If the real part is positive, the system is unstable; if the real part is negative, the system is stable. Multi-degree-of-freedom systems with time-dependent parameters can be expressed in the following form:

$$\dot{\boldsymbol{x}} = \boldsymbol{A}(t)\boldsymbol{x}, \quad \boldsymbol{A}(t) = \boldsymbol{A}(t+T), \quad T = \frac{2\pi}{\Omega} \tag{2.35}$$

where $\boldsymbol{x}$ is a vector with length $2N$, $\boldsymbol{A}(t)$ is a $2N$ x $2N$ periodic matrix and Ω is the oscillation frequency. Floquet's theorem states that the fundamental matrix solution $\boldsymbol{U}(t)$ can be expressed as:

$$\boldsymbol{U}(t) = \boldsymbol{P}(t)\text{exp}(t\boldsymbol{F}) \tag{2.36}$$

where $\boldsymbol{P}(t) = \boldsymbol{P}(t+T)$ is a $2N$ x $2N$ matrix periodic in time, and $\boldsymbol{F}$ is a complex-valued, time independent $2N$ x $2N$ matrix. The Floquet eigenvalues of matrix $\boldsymbol{F}$ determine the stability of the system. If any of the Floquet eigenvalues has a positive real part and is greater than zero, then $\boldsymbol{U}(t)$ grows over time, indicating instability. If all Floquet eigenvalues are negative, the system remains stable.

The Floquet eigenvalues can be determined numerically by introducing a state transition matrix in the following form:

$$\boldsymbol{\Phi}(t, t_0) = \boldsymbol{U}(t)\boldsymbol{U}^{-1}(t_0) \tag{2.37}$$

The fundamental matrix solution is periodic in time. Therefore, evaluating the system's response over one period T is sufficient. After substituting $t = T$ and $t_0 = 0$ into equation 2.36. This expression can then be substituted into equation 2.37, resulting in:

$$\boldsymbol{\Phi}(T, 0) = \boldsymbol{P}(T)\mathsf{exp}(T\boldsymbol{F})\boldsymbol{P}^{-1}(0) = \boldsymbol{P}(0)\mathsf{exp}(T\boldsymbol{F})\boldsymbol{P}^{-1}(0) \tag{2.38}$$

The beauty of linear systems is that the stability is independent of the initial conditions. Thus, any initial conditions can be selected to evaluate the Floquet eigenvalues of matrix $\boldsymbol{F}$. For convenience, the identity matrix is chosen as the initial conditions, resulting in $\boldsymbol{U}(0) = \boldsymbol{P}(0) = \boldsymbol{I}$. This simplifies equation 2.38 to:

$$\boldsymbol{\Phi}(T, 0) = \mathsf{exp}(T\boldsymbol{F}) \tag{2.39}$$

This final expression is referred to as the Floquet multiplier. A system is considered stable when the absolute value of the Floquet multiplier is smaller than 1, and unstable when it exceeds 1.

The exponential harmonic balance method can be used in combination with Floquet's theorem, using the principle that the transition between stable and unstable states occurs when the absolute value of the Floquet multiplier equals 1. To determine the system's stability state, the solutions of the field quantities can be written as non-decreasing and bounded solutions, aligning with Floquet's theorem:

$$x(t) = \left(\sum_{k=-N}^{N} X_k \mathsf{exp}(i\omega_k t) \right) \mathsf{exp}(i\omega t) \tag{2.40}$$

$$\omega_k = k\omega_1$$

where $\mathsf{exp}(i\omega t)$ is the Floquet multiplier evaluated at 1, and N denotes the number of harmonics considered, and ω_1 is the excitation frequency. After setting up the assumed solutions for all field quantities, they can be substituted in the equations of motion. To create a square system of equations, the equations of motion are multiplied with $\mathsf{exp}(i\omega_m t)$ and integrated over T. This approach groups the terms with the same components, which is similar to the orthogonality theorem. To assess the system's stability, the determinant of the resulting matrix must be set to zero, which allows solving for the unknown natural frequency ω. In chapter 4, this theorem is applied to our specific problem.

3

Stability of a Continuously Supported Euler-Bernoulli Beam with an Electromagnetically Suspended Moving Mass and Constant Aeroelastic Force

3.1. Model Formulation

The system consists of a continuously supported, infinitely long Euler-Bernoulli. The beam has a bending stiffness, EI, and a mass density per unit length ρA. The foundation includes both springs, k_b, and dashpots, c_b. The vehicle is modelled as a point mass, M, and is suspended from the beam via an electromagnetic force, $F_{EM}(t)$, which operates in attraction. The mass moves in the x-direction at a constant velocity v. Since the tube is not completely vacuum-sealed, the vehicle experiences a constant aeroelastic force with the same velocity as the vehicle's. Gravitational acceleration is denoted by g. The beam's displacement is a function of both space and time denoted by $w(x,t)$. The displacement of the mass is measured relative to the beam and depends only on time and is denoted by $z(t)$. This system is referred to as system 1 through the thesis.

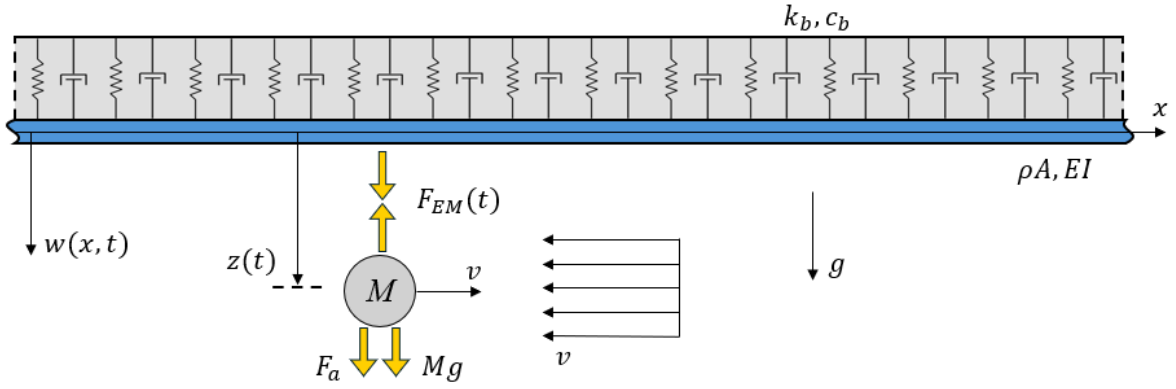

Figure 3.1: System schematics - Continuously supported infinite Euler-Bernoulli beam subjected to an electromagnetically suspended moving mass under a constant aeroelastic force

The equations of motion of this system are given in Chapter 2 and summarised here. The moving reference frame is used for convenience [6]. ξ is the position of the mass and is expressed as $\xi = x - vt$. The displacement of the beam is represented in the moving reference frame as $w(\xi, t)$.

$$\rho A(\ddot{w} - 2v\dot{w} + v^2 w'') + EIw'''' + c_b(\dot{w} - vw') + k_b w = F_{EM}(t)\delta(\xi) \tag{3.1}$$

$$M\ddot{z}(t) = -F_{EM}(t) + Mg + \mu\dot{z}(t) \tag{3.2}$$

$$F_{EM}(t) = C\frac{I^2(t)}{\Delta^2(t)} \tag{3.3}$$

$$\dot{I}(t) + \frac{\Delta(t)}{2C}\left(R - 2C\frac{\dot{\Delta}(t)}{\Delta^2(t)}\right)I(t) = \frac{\Delta(t)}{2C}U(t) \tag{3.4}$$

$$U(t) = U_{ss} + K_p(\Delta(t) - \Delta_{ss}) + K_d\dot{\Delta}(t) \tag{3.5}$$

where

$$\Delta(t) = z(t) - w_0(t) \tag{3.6}$$

$$\Delta_{ss} = z_{ss} - w_{0,ss} \tag{3.7}$$

$$\mu = \left|\frac{1}{2}\rho_{air}vA_v\left(\frac{\partial C}{\partial \alpha}\right)_0\right| \tag{3.8}$$

The electromagnetic force, $F_{EM}(t)$ depends on the constant C, the current I, and the air gap Δ, which is the distance between the mass and the beam. Therefore, the displacement of the beam at the location of the moving mass is considered, denoted as $w_0 = w(\xi = 0)$. The aeroelastic term, μ acts as negative damping, injecting energy into the system. It is assumed that the vehicle's horizontal velocity is significantly larger than its vertical velocity, allowing the use of the given formula for μ. Moreover, it is assumed that the vehicle moves at a constant velocity.

This model is a simplification of reality. The tube and columns are not included explicitly. Their effects are included in the beam's mass and the foundation stiffness. This approach follows that in the paper of Fărăgău et al. [6]. The tube is modelled as a beam with an additional 10% to account for the mass of the guidance system. The mass of the columns is also considered in the calculation of the beam mass, where 10% of the column mass is distributed over the span length. The stiffness of the viscoelastic foundation depends solely on the columns. To account for the soil's flexibility, 50% of the column stiffness is considered. This stiffness is then divided by the span length to model the continuous foundation.

3.2. Solution Method

The system is nonlinear because of the electromagnetic force. To analyse the stability of the system, the linearised form is used. An equilibrium point is selected for the linearisation because the system can have multiple equilibrium points. Around the steady state, a perturbation is added, denoted by the subscript "tr", which is applied to describe the system's response and analyse its stability.

$$w_0(t) = w_{0,ss} + w_{0,tr}(t) \tag{3.9}$$

$$F_{EM}(t) = F_{ss} + F_{tr}(t) \tag{3.10}$$

$$z(t) = z_{ss} + z_{tr}(t) \tag{3.11}$$

$$I(t) = I_{ss} + I_{tr}(t) \tag{3.12}$$

Equations 4.3 - 4.5 are linearised using Taylor expansion. For the displacement of the beam, Green's function is applied, leading to the following expressions:

$$w_{0,tr}(\tau) = \int_0^t G_0(t-\tau)F_{tr}(\tau)\,d\tau \tag{3.13}$$

$$M\ddot{z}_{tr}(\tau) = -F_{tr}(\tau) + \mu\dot{z}_{tr}(\tau) \tag{3.14}$$

$$F_{tr}(\tau) = \frac{2CI_{ss}^2}{\Delta_{ss}^3}\left(\frac{\Delta_{ss}}{I_{ss}}I_{tr}(\tau) - z_{tr}(\tau) + w_{0,tr}(\tau)\right) \tag{3.15}$$

$$\dot{I}_{tr}(\tau) = \frac{\Delta_{ss}}{2C}\Big(-I_{tr}(\tau)R + K_p(z_{tr}(\tau) - w_{0,tr}(\tau)) + \left(K_d + \frac{2CI_{ss}}{\Delta_{ss}^2}\right)(\dot{z}_{tr}(\tau) - \dot{w}_{0,tr}(\tau))\Big) \tag{3.16}$$

The equations are linearised around the equilibrium point, (z_{ss}, I_{ss}). When the system is disturbed near the equilibrium point, its response depends on the stability of that point. In the case of a stable equilibrium point, the system returns to equilibrium after disturbance. However, if the equilibrium point is unstable, the system diverges. By examining the eigenvalues at this point, a stability analysis can be performed, reducing the complexity of the problem.

The stability analysis is conducted through an eigenvalue analysis in the Laplace domain. First, equations 3.13 - 3.16 are transformed into the Laplace domain. After this, the equations are expressed in matrix form. In the Laplace domain, the equations of motion are noted as:

$$\hat{w}_{0,tr} = \hat{G}_{EB}(s)\hat{F}_{tr}(s) \tag{3.17}$$

$$\hat{F}_{tr}(s) = \frac{2CI_{ss}^2}{\Delta_{ss}^3}\hat{w}_{0,tr} - \frac{2CI_{ss}^2}{\Delta_{ss}^3}\hat{z}_{tr} + \frac{2CI_{ss}}{\Delta_{ss}^2}\hat{I}_{tr} \tag{3.18}$$

$$\frac{2CI_{ss}^2}{\Delta_{ss}^3}\hat{w}_{0,tr} + \left(Ms^2 - \frac{2CI_{ss}^2}{\Delta_{ss}^3} - \mu s\right)\hat{z}_{tr} + \frac{2CI_{ss}}{\Delta_{ss}^2}\hat{I}_{tr} = M(sz_{0,tr} + \dot{z}_{0,tr}) \tag{3.19}$$

$$\begin{aligned}\left(\frac{K_p\Delta_{ss}^2 + (K_d\Delta_{ss}^2 + 2CI_{ss})s}{2C\Delta_{ss}}\right)\hat{w}_{0,tr} - \left(\frac{K_p\Delta_{ss}^2 + (K_d\Delta_{ss}^2 + 2CI_{ss})s}{-2C\Delta_{ss}}\right)\hat{z}_{tr} \\ + \left(s + \frac{\Delta_{ss}R}{2C}\right)\hat{I}_{tr} = \frac{K_d\Delta_{ss}^2 + 2CI_{ss}}{2C\Delta_{ss}}\left(z_{0,tr} - w_{0,tr}\right) + I_{0,tr}\end{aligned} \tag{3.20}$$

The system of equations, in matrix form, is expressed as:

$$\begin{pmatrix} 1 - \hat{G}_{EB}(s)\frac{2CI_{ss}^2}{\Delta_{ss}^3} & \hat{G}_{EB}(s)\frac{2CI_{ss}^2}{\Delta_{ss}^3} & -\hat{G}_{EB}(s)\frac{2CI_{ss}}{\Delta_{ss}^2} \\ \frac{2CI_{ss}^2}{\Delta_{ss}^3} & Ms^2 - \frac{2CI_{ss}^2}{\Delta_{ss}^3} - \mu s & \frac{2CI_{ss}}{\Delta_{ss}^2} \\ \frac{K_p\Delta_{ss}^2 + (K_d\Delta_{ss}^2 + 2CI_{ss})s}{2C\Delta_{ss}} & \frac{K_p\Delta_{ss}^2 + (K_d\Delta_{ss}^2 + 2CI_{ss})s}{-2C\Delta_{ss}} & s + \frac{\Delta_{ss}R}{2C} \end{pmatrix} \begin{pmatrix} \hat{w}_{0,tr} \\ \hat{z}_{tr} \\ \hat{I}_{tr} \end{pmatrix} = \begin{pmatrix} 0 \\ M(sz_{0,tr} + \dot{z}_{0,tr}) \\ \Psi \end{pmatrix}$$

$$\Psi = \frac{K_d\Delta_{ss}^2 + 2CI_{ss}}{2C\Delta_{ss}}\left(z_{0,tr} - w_{0,tr}\right) + I_{0,tr}$$

The characteristic equation is derived by equating the determinant of the matrix to zero. In the matrix, $z_{0,tr}$, $\dot{z}_{0,tr}$ and $I_{0,tr}$ are the initial conditions of the mass and current at $\tau = 0$. Since the stability is independent of the initial conditions, it is assumed that the mass and beam are initially undisturbed. The eigenvalues must be computed numerically since the characteristic equation is neither a polynomial nor a transcendental equation, which implies that there are a finite number of roots. To determine the eigenvalues, Matlab's built-in function $fsolve$ is used. This solver makes use of the Newton-Raphson method to find the zero crossings. Therefore, it requires initial guesses for s to begin the search for the solutions. Combinations of K_p and K_d with a positive real part are stored to form the stability boundary.

3.2.1. Green's Function

The Green's function represents the system's response to a Dirac delta pulse. The advantage of using Green's functions is that they are system-dependent. This allows for the determination of the system's response to any applied force. The Green's function is derived using Cauchy's integral theorem.

The Green's function is derived in the Laplace domain. First, the Laplace transform with respect to t and the Fourier transform with respect to ξ are applied. The boundary conditions are that the system's response is zero at infinity, because of the viscoelastic foundation. Since the stability is independent of the initial conditions, it is assumed that $w(\xi, 0) = \dot{w}(\xi, 0) = 0$. The Fourier and Laplace transform are [19]:

$$W_{k,s}(k,s) = \int_{-\infty}^{\infty} V_s(\xi,s)\mathsf{exp}(-ik\xi)d\xi, \quad V_s(\xi,s) = \int_{-\infty}^{\infty} w(\xi,t)\mathsf{exp}(-st)dt \tag{3.21}$$

Applying these transformations to equation 3.1 results in the following expression:

$$\left(k^4 - \frac{\rho A v^2}{EI}k^2 - \frac{2i\rho Avs + ic_b v}{EI}k + \frac{\rho As^2 + k_b + c_b s}{EI}\right)W_{k,s}(k,s) = \frac{\hat{F}_{EM}(s)}{EI} \tag{3.22}$$

The solution in the Laplace domain is obtained by applying the inverse Fourier Transform to the expressions, resulting in:

$$V(\xi,s) = \frac{\hat{F}_{EM}(s)}{2\pi EI}\int_{-\infty}^{\infty} \frac{\mathsf{exp}(ik\xi)}{D(k,s)}dk \tag{3.23}$$

where

$$D(k,s) = k^4 - \frac{\rho A v^2}{EI}k^2 - \frac{2i\rho Avs + ic_b v}{EI}k + \frac{\rho As^2 + k_b + c_b s}{EI} \tag{3.24}$$

Since the response is determined at the contact point, $\xi = 0$ is substituted in equation 3.23, leading to the following result:

$$V(0,s) = \hat{F}_{EM}(s)g_{EB}(0,s), \quad g_{EB}(0,s) = \frac{1}{2\pi EI}\int_{-\infty}^{\infty} \frac{1}{D(k,s)}dk \tag{3.25}$$

$g_{EB}(0,s)$ is the Green's function for the Euler-Bernoulli beam in the Laplace domain, which, as expected, is independent of the applied force. The integral can be computed using Cauchy's integration formula, giving the following result:

$$g_{EB}(0,s) = \frac{i}{EI} \sum_{n=1}^{m} \lim_{k \to k_n} \frac{k - k_n}{(k-k_1)(k-k_2)(k-k_3)(k-k_4)} \tag{3.26}$$

The equation $D(k,s) = 0$ has four roots, denoted as k, and can be located in the complex plane as illustrated in Figure 3.2. At $\xi = 0$, the response in front of and behind the moving load is symmetric, this allows for the use of either of the planes for the contour integration. For these calculations, only the poles in the upper half of the plane are considered. In the summation, m is set to two, reflecting the number of poles used in the contour integration.

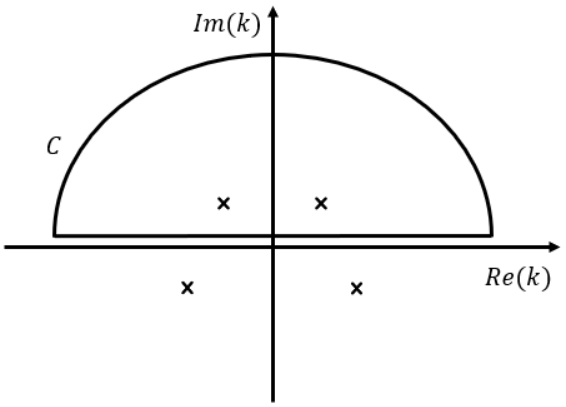

Figure 3.2: Contour C in the upper half of the complex plane with an example of the k-roots

4

Irregular Euler-Bernoulli Beam with Continuous Support under an Electromagnetically Suspended Moving Mass and Constant Aeroelastic Force

4.1. Model Formulation

Figure 4.1 illustrates the irregular Euler-Bernoulli beam, where the only difference compared to system 1 is the addition of irregularities in the guideway. Most equations remain the same. Time-dependency is now introduced in Δ_{ss}, I_{ss} and U_{ss}. This system is referred to as system 2. The irregularity is characterised by a cosine function.

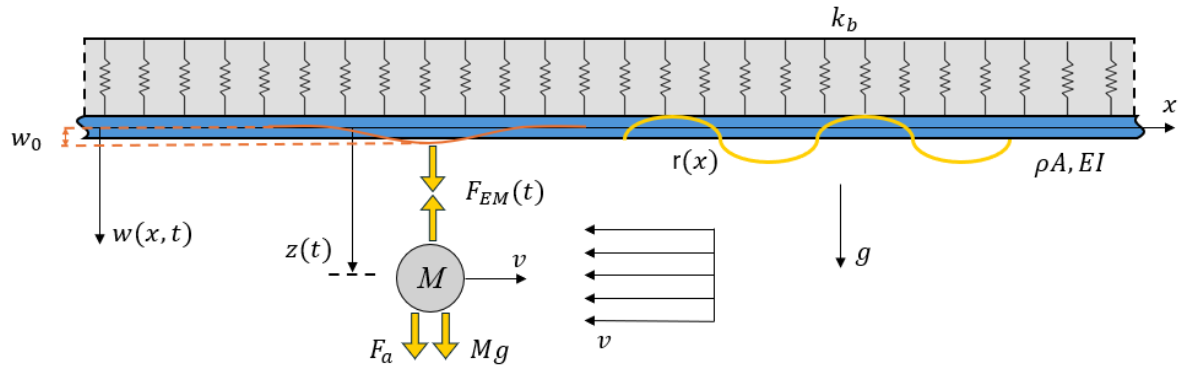

Figure 4.1: System schematics - Continuously supported irregular infinite Euler-Bernoulli beam subjected to an electromagnetically suspended moving mass under a constant aeroelastic force

$$r(x) = \frac{1}{2}A(1 - cos(\kappa x)), \quad \kappa = \frac{2\pi}{L} \tag{4.1}$$

The irregular guideway profile influences the air gap at the contact point, $x = vt$. The equations of motion now become:

$$\rho A(\ddot{w} - 2v\dot{w} + v^2 w'') + EIw'''' + k_b w = F_{EM}(t)\delta(x - vt) \tag{4.2}$$

$$M\ddot{z}(t) = -F_{EM}(t) + Mg + \mu\dot{z}(t) \tag{4.3}$$

$$F_{EM}(t) = C\frac{I^2(t)}{\Delta^2(t)} \tag{4.4}$$

$$\dot{I}(t) + \frac{\Delta(t)}{2C}\left(R - 2C\frac{\dot{\Delta}(t)}{\Delta^2(t)}\right)I(t) = \frac{\Delta(t)}{2C}U(t) \tag{4.5}$$

$$U(t) = U_{ss} + K_p(\Delta(t) - \Delta_{ss}(t)) + K_d(\dot{\Delta}(t) - \dot{\Delta}_{ss}(t)) \tag{4.6}$$

$$\Delta(t) = z(t) - w_0(t) - r_0(t) \tag{4.7}$$

$$w_0(t) = w(x = vt, t) \tag{4.8}$$

$$r_0(t) = r(x = vt) = \frac{1}{2}A(1 - cos(\omega_1 t)), \quad \omega_1 = \kappa v = \frac{2\pi v}{L} \tag{4.9}$$

$$\Delta_{ss}(t) = z_{ss} - w_{0,ss} - r_0(t) \tag{4.10}$$

Note that z_{ss} and $w_{0,ss}$ are time-independent. $w_{0,ss}$ is the steady state response of an Euler-Bernoulli beam under a moving constant load. Assuming that z_{ss} is constant, the steady-state field parameters are given in the following form:

$$w_{0,ss} = \frac{Mg}{2\pi vEI}\int_{-\infty}^{\infty}\frac{1}{\Lambda(\omega, v)}, \quad \Lambda(\omega, v) = \left(\frac{\omega}{v}\right)^4 - \frac{\rho A}{EI}\omega^2 + \frac{k_b}{EI} \tag{4.11}$$

$$I_{ss}(t) = \sqrt{\frac{Mg\Delta_{ss}^2(t)}{C}} \tag{4.12}$$

$$U_{ss}(t) = RI_{ss}(t) \tag{4.13}$$

The system without the constant aeroelastic force is also analysed. Figure 4.2 illustrates the system.

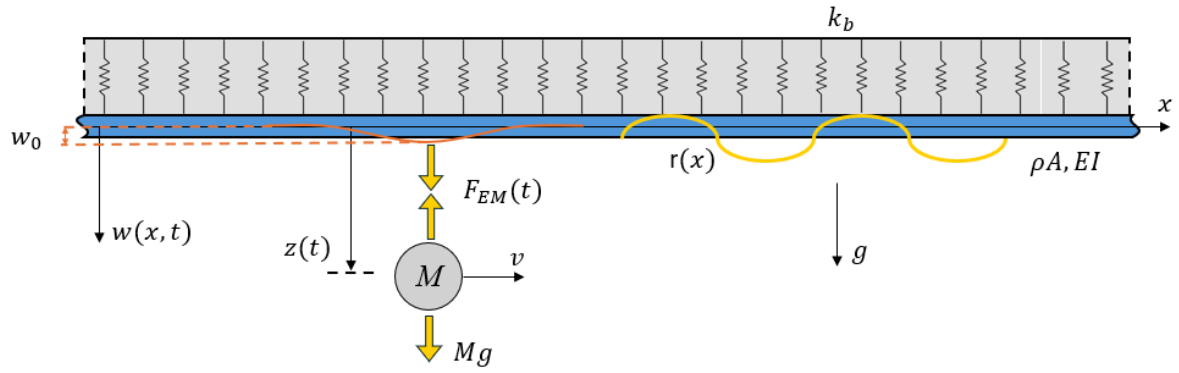

Figure 4.2: System schematics - Continuously supported irregular infinite Euler-Bernoulli beam subjected to an electromagnetically suspended moving mass

The only difference in the equations of motion for this system is the absence of the constant aeroelastic force in the equation of motion of the mass:

$$M\ddot{z}(t) = -F_{EM}(t) + Mg \tag{4.14}$$

4.2. Solution Method

System 2 is solved using a combination of Floquet's theorem and the exponential harmonic balance method. The linearised equations for system 2 are noted as:

$$\rho A\ddot{w}_{tr} + EIw''''_{tr} + k_b w_{tr} = F_{tr}\delta(x - vt) \tag{4.15}$$

$$M\ddot{z}_{tr}(t) = -F_{tr}(t) + \mu\dot{z}_{tr}(t) \tag{4.16}$$

$$F_{tr}(t) = \frac{2CI_{ss}^2(t)}{\Delta_{ss}^3(t)}\left(\frac{\Delta_{ss}(t)}{I_{ss}(t)}I_{tr}(t) - \Delta_{tr}(t)\right) \tag{4.17}$$

$$\begin{aligned}\dot{I}_{tr}(t) = \left(-\frac{R\Delta_{ss}(t)}{2C} + \frac{\dot{\Delta}_{ss}(t)}{\Delta_{ss}(t)}\right)I_{tr}(t) + \left(\frac{K_p\Delta_{ss}(t)}{2C} - \frac{\dot{\Delta}_{ss}(t)I_{ss}(t)}{\Delta_{ss}(t)}\right)\Delta_{tr}(t) \\ + \left(\frac{K_d\Delta_{ss}(t)}{2C} + \frac{I_{ss}(t)}{\Delta_{ss}(t)}\right)\dot{\Delta}_{tr}(t)\end{aligned} \tag{4.18}$$

where

$$\Delta_{tr}(t) = z_{tr}(t) - w_{0,tr}(t) \tag{4.19}$$

The solutions for the field parameters are assumed in a non-decreasing and bounded form in line with Floquet's theorem, as described in chapter 2. The solutions for the field parameters are expressed as:

$$z_{tr}(t) = \left(\sum_{k=-N}^{N} Z_k \exp(i\omega_k t)\right)\exp(i\omega t) \tag{4.20}$$

$$F_{tr}(t) = \left(\sum_{k=-N}^{N} F_k \exp(i\omega_k t)\right)\exp(i\omega t) \tag{4.21}$$

$$w_{0,tr}(t) = \left(\sum_{k=-N}^{N} W_k \exp(i\omega_k t)\right)\exp(i\omega t) \tag{4.22}$$

$$I_{tr}(t) = \left(\sum_{k=-N}^{N} I_k \exp(i\omega_k t)\right)\exp(i\omega t) \tag{4.23}$$

To find the stability boundary, the Floquet multiplier is evaluated at 1, since this value represents the threshold value between stability and instability. In the equations, the natural frequency ω is unknown, and ω_k is:

$$\omega_k = k\omega_1 = k\frac{2\pi v}{L} \tag{4.24}$$

The assumed solutions can be expressed in a form that satisfies the equations of motion for both the beam and the mass.

$$z_{tr}(t) = \sum_{k=-N}^{N} Z_k \exp(i\bar{\omega}_k t) \tag{4.25}$$

$$F_{tr}(t) = \sum_{k=-N}^{N} F_k \exp(i\bar{\omega}_k t) = \sum_{k=-N}^{N} \left(\bar{\omega}_k^2 M + i\mu\bar{\omega}_k\right) Z_k \exp(i\bar{\omega}_k t) \tag{4.26}$$

$$w_{0,tr}(t) = \sum_{k=-N}^{N} F_k w_k \exp(i\bar{\omega}_k t) = \sum_{k=-N}^{N} \left(\bar{\omega}_k^2 M + i\mu\bar{\omega}_k\right) Z_k w_k \exp(i\bar{\omega}_k t) \tag{4.27}$$

$$I_{tr}(t) = \sum_{k=-N}^{N} I_k \exp(i\bar{\omega}_k t) \tag{4.28}$$

Note that $\bar{\omega}_k = \omega + \omega_k$. In the equations, w_k is the response of an Euler-Bernoulli beam subjected to a moving oscillatory unit load, which can be derived analytically, using Cauchy's integration formula.

$$w_k(x = vt, t) = \frac{1}{2\pi v EI} \exp(i\bar{\omega}_k t) \int_{-\infty}^{\infty} \frac{1}{\Lambda(\omega, \bar{\omega}_k, v)}, \quad \Lambda(\omega, \bar{\omega}_k, v) = \left(\frac{\omega - \bar{\omega}_k}{v}\right)^4 - \frac{\rho A}{EI}\omega^2 + \frac{k_b}{EI} \tag{4.29}$$

The unknown variables in the equations are F_k, I_k and ω. These unknowns can be determined from the expressions 4.17 and 4.18. The expressions can be reformulated to:

$$F_{tr}(t) = f_1(t) I_{tr} - f_2(t)(z_{tr} - w_{0,tr}) \tag{4.30}$$

$$\dot{I}_{tr} + f_3(t) I_{tr} = f_4(t)(z_{tr} - w_{0,tr}) + f_5(t)(\dot{z}_{tr} - \dot{w}_{0,tr}) \tag{4.31}$$

where

$$f_1(t) = \frac{2C I_{ss}(t)}{\Delta_{ss}^2(t)} \qquad f_4(t) = \frac{K_p \Delta_{ss}(t)}{2C} - \frac{\dot{\Delta}_{ss}(t) I_{ss}(t)}{\Delta_{ss}^2(t)} \tag{4.32}$$

$$f_2(t) = \frac{2C I_{ss}^2(t)}{\Delta_{ss}^3(t)} \qquad f_5(t) = \frac{K_d \Delta_{ss}(t)}{2C} + \frac{I_{ss}(t)}{\Delta_{ss}(t)} \tag{4.33}$$

$$f_3(t) = \frac{R\Delta_{ss}^2(t) - 2C\dot{\Delta}_{ss}(t)}{2C\Delta_{ss}(t)} \tag{4.34}$$

Substituting the assumed solutions into equations 4.30 and 4.31 results in the following equations:

$$\sum_{k=-N}^{N} F_k \exp(i\bar{\omega}_k t) = f_1(t) \sum_{k=-N}^{N} I_k \exp(i\bar{\omega}_k t) - f_2(t) \left(\sum_{k=-N}^{N} \left(\frac{1}{M\bar{\omega}_k^2 + i\mu\bar{\omega}_k} - w_k \right) F_k \exp(i\bar{\omega}_k t) \right) = 0 \tag{4.35}$$

$$\sum_{k=-N}^{N}(i\bar{\omega}_k + f_3(t))I_k\text{exp}(i\bar{\omega}_k t) = f_4(t)\left(\sum_{k=-N}^{N}\left(\frac{1}{M\bar{\omega}_k^2 + i\mu\bar{\omega}_k} - w_k\right)F_k\text{exp}(i\bar{\omega}_k t)\right) + f_5(t)\left(\sum_{k=-N}^{N}\left(\frac{1}{M\bar{\omega}_k^2 + i\mu\bar{\omega}_k} - w_k\right)i\bar{\omega}_k F_k\text{exp}(i\bar{\omega}_k t)\right) = 0 \tag{4.36}$$

The Floquet multiplier can be factored out and dropped because it is present in all the terms, simplifying the equations to:

$$\sum_{k=-N}^{N}F_k\text{exp}(i\omega_k t) = f_1(t)\sum_{k=-N}^{N}I_k\text{exp}(i\omega_k t) - f_2(t)\left(\sum_{k=-N}^{N}\left(\frac{1}{M\bar{\omega}_k^2 + i\mu\bar{\omega}_k} - w_k\right)F_k\text{exp}(i\omega_k t)\right) = 0 \tag{4.37}$$

$$\sum_{k=-N}^{N}(i\bar{\omega}_k + f_3(t))I_k\text{exp}(i\omega_k t) = f_4(t)\left(\sum_{k=-N}^{N}\left(\frac{1}{M\bar{\omega}_k^2 + i\mu\bar{\omega}_k} - w_k\right)F_k\text{exp}(i\omega_k t)\right) + f_5(t)\left(\sum_{k=-N}^{N}\left(\frac{1}{M\bar{\omega}_k^2 + i\mu\bar{\omega}_k} - w_k\right)i\bar{\omega}_k F_k\text{exp}(i\omega_k t)\right) = 0 \tag{4.38}$$

The natural frequency ω is unknown, except at parametric resonance. The following choices are made:

$$T_1 : \omega = 0 \tag{4.39}$$

$$T_2 : \omega = \frac{1}{2}\omega_1 \tag{4.40}$$

For the remaining part of the stability boundary, ω is unknown. Therefore, a squared system of equations is formed using expressions 4.37 and 4.38. These expressions are multiplied by $\text{exp}(i\omega_m t)$, where $m = -N...N$, and integrated over the period $T = \frac{2\pi}{\omega_1}$. This procedure isolates terms where $k = m$ which results in a fully populated matrix. By setting the matrix's determinant to zero, the unknown frequency ω can be determined. Matlab is used to perform these calculations.

The parameters used in this research are presented in Table 4.1. These values are obtained from the paper of Fărăgău et al. [6] and company Hardt Hyperloop [8].

Parameter	Symbol	Value	Unit
Mass per unit length	ρA	1.44×10^{3}	kg/m
Bending stiffness	EI	2.50×10^{10}	Nm^2
Foundation damping	c_b	2.00×10^{4}	$\mathrm{Ns/m}^2$
Foundation stiffness	k_b	2.76×10^{7}	$\mathrm{N/m}^2$
Vehicle mass	M	7650	kg
Total resistance of coil	R	9.71	Ohm
Constant	C	0.05	Nm^2/A^2
Desired airgap	z_{ss}	0.015	m
Initial voltage	U_{ss}	177.97	V
Air density	ρ_{air}	1.29	$\mathrm{kg/m}^3$
Front area of vehicle	A_v	5.73	m^2
Angular dependent air coefficient	$\left(\frac{\partial C}{\partial \alpha}\right)_0$	-1.00	$-$
Surface roughness amplitude	A	0.008	m

Table 4.1: Parameter values

5

Electromagnetically Suspended Mass on an Oscillating Base Under a Varying Aeroelastic Force

5.1. Model Formulation

Figure 5.1 illustrates the third system, where a Hyperloop vehicle with mass M is suspended from an oscillating rigid base with frequency Ω, through the electromagnetic force $F_{EM}(t)$. The mass is subjected to a time-varying airflow, which introduces a time-dependent aeroelastic force $F_a(t)$. This system is referred to as system 3. The equations of motion for the electromagnetic force are similar to those of systems 1 and 2. However, due to the oscillating base, the air gap distance varies, which also changes the equation for the voltage.

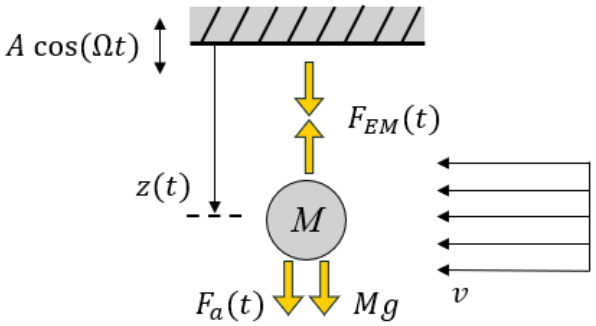

Figure 5.1: System schematics - Electromagnetically suspended mass subjected to a modulated aeroelastic force

$$\Delta(t) = z(t) - Acos(\Omega t) \tag{5.1}$$

$$\Delta_{ss}(t) = z_{ss} - Acos(\Omega t) \tag{5.2}$$

$$U(t) = U_{ss} + K_p(\Delta(t) - \Delta_{ss}(t)) + K_d(\dot{\Delta}(t) - \dot{\Delta}_{ss}(t)) \tag{5.3}$$

With the addition of the oscillating base, the system has a time-dependent parameter, introducing the possibility of parametric instability.

In reality, the airflow is not constant. In this system, the mass is subjected to an oscillating aeroelastic force. Interestingly, dolphins are capable of changing their body size to increase or decrease

their frontal area, which helps maintain a laminar flow around their bodies and regulate body heat [29]. Inspired by this concept, a variable frontal area of the Hyperloop could potentially be explored to mitigate the effects caused by the aeroelastic oscillations. This concept might be applied in the future as technology continues to advance. The oscillations of the aeroelastic force are represented by the aeroelastic parameter, μ:

$$\mu(t) = \mu_1 + \mu_2 cos(\Omega t) \tag{5.4}$$

It is important to remember that the aeroelastic force acts as a destabilising input. When introducing the oscillations to μ, it is essential that μ does not become negative. This would imply positive damping, which could have a stabilising effect on the system. However, for completeness, the case where μ_2 is bigger than μ_1 is also analysed.

5.2. Solution Method

The stability of system 3 is analysed using Floquet's theorem. Compared to system 1, the linearised equations for system 3 are slightly different because of the time-dependent parameters. The equations are noted as:

$$M\ddot{z}_{tr}(t) = -F_{tr}(t) + \mu(t)\dot{z}_{tr}(t) \tag{5.5}$$

$$F_{tr}(t) = \frac{2CI_{ss}^2(t)}{\Delta_{ss}^3(t)}\left(\frac{\Delta_{ss}(t)}{I_{ss}(t)}I_{tr}(t) - z_{tr}(t)\right) \tag{5.6}$$

$$\begin{aligned}\dot{I}_{tr}(t) = \left(\frac{K_p\Delta_{ss}(t)}{2C} - \frac{\dot{\Delta}_{ss}(t)I_{ss}(t)}{\Delta_{ss}^2(t)}\right)z_{tr}(t) + \left(\frac{K_d\Delta_{ss}(t)}{2C} + \frac{I_{ss}(t)}{\Delta_{ss}(t)}\right)\dot{z}_{tr}(t) \\ + \left(-\frac{R\Delta_{ss}(t)}{2C} + \frac{\dot{\Delta}_{ss}(t)}{\Delta_{ss}(t)}\right)I_{tr}(t)\end{aligned} \tag{5.7}$$

The equations are written in state-space form, resulting in the following matrix:

$$\begin{pmatrix}\dot{z}_{tr}(t)\\ \ddot{z}_{tr}(t)\\ \dot{I}_{tr}(t)\end{pmatrix} = \begin{pmatrix}0 & 1 & 0\\ \frac{2CI_{ss}^2}{M\Delta_{ss}^3} & \frac{\mu}{M} & -\frac{2CI_{ss}}{M\Delta_{ss}^2}\\ \frac{K_p\Delta_{ss}}{2C} - \frac{\dot{\Delta}_{ss}I_{ss}(t)}{\Delta_{ss}^2} & \frac{K_d\Delta_{ss}}{2C} + \frac{I_{ss}}{\Delta_{ss}} & -\frac{R\Delta_{ss}}{2C} + \frac{\dot{\Delta}_{ss}}{\Delta_{ss}}\end{pmatrix}\begin{pmatrix}z_{tr}(t)\\ \dot{z}_{tr}(t)\\ I_{tr}(t)\end{pmatrix}$$

According to Floquet's theorem, analysing the system's response after one period is sufficient to determine the stability. A 3x3 identity matrix is used for the initial conditions since the initial conditions do not change the system's stability. Using Matlab's built-in ODE45 solver, the response at T is determined, where $T = \frac{2\pi}{\Omega}$. The final step is to calculate the eigenvalues and look for the combinations of K_p and K_d where at least one of the eigenvalues has a positive real part.

6

Results and Discussion

6.1. Results used for Comparison

In this section, the results from Fărăgău et al. [6] and Paul et al. [27] (not published yet) are presented as the baseline for comparison made later in this chapter. These studies are used as a reference to analyse the effects of the aeroelastic force and the irregular guideway profile on the system's stability.

6.1.1. Stability of a Continuously Supported Euler-Bernoulli Beam with an Electromagnetically Suspended Moving Mass

In the paper presented by Fărăgău et al. [6], it was observed that the system has five eigenvalues, of which three determine the system's stability. Figure 6.1 illustrates the eigenvalues across the velocity spectrum. Two of the five eigenvalues only appear within $v \approx 0.7 - 1.3 v_{cr}$. The eigenvalue analysis cannot fully describe the infinite guideway coupled with the moving vehicle because the integrals along the branch cuts also contribute to the system's dynamic behaviour. The eigenvalues provide information about the system's stability and the rate at which stability changes as the velocity varies. The lowest real part of the complex-valued eigenvalues is observed at approximately $0.7 v_{cr}$, indicating that as the vehicle initially accelerates, the system's stability improves. The system remains stable up to a velocity of approximately $1.3 v_{cr}$, where the real parts of the complex-valued eigenvalues become positive. The loss of stability happens through a supercritical Hopf bifurcation. As the velocity continues to increase, stability is regained at $v \approx 1.7 v_{cr}$.

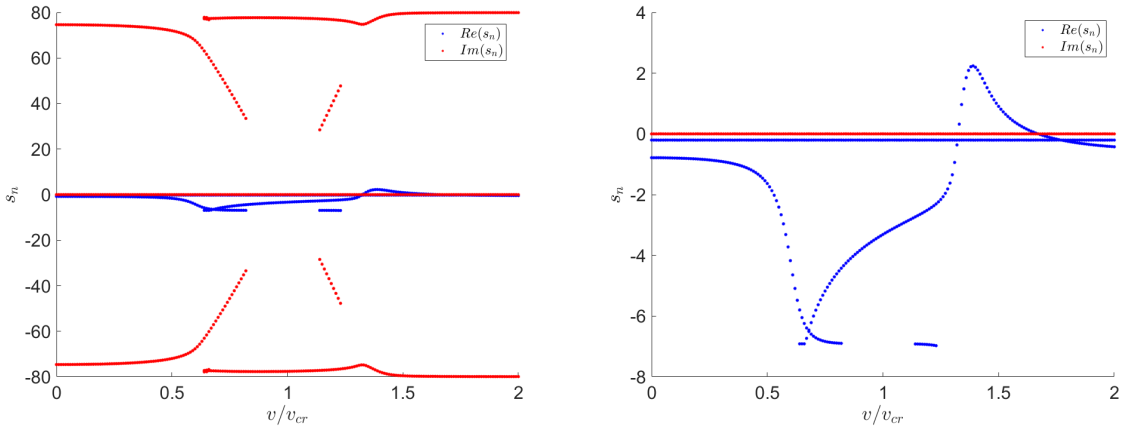

(a) Real part and Imaginary part

(b) Close up of the real part of the eigenvalues

Figure 6.1: The eigenvalues versus relative velocity of the vehicle. K_p = 2.0×10^4 V/m, K_d = 4.0×10^4 Vs/m

Figure 6.2 illustrates the stability planes obtained by Fărăgău et al. [6]. The grey areas indicate instability and the white areas indicate stability. For velocities in the range of $1.3 - 2.0v_{cr}$, the unstable domain lies to the right of the stability boundary. For all velocities, there is a minimum value for K_p below which the system is always unstable. The controller is not able to respond quickly enough to counter the gravitational pull of the vehicle. At subcritical velocities, as the vehicle accelerates, it benefits the stability of the system by reducing the unstable domain. This trend aligns with the behaviour observed in the eigenvalues. However, from $0.8v_{cr}$ onwards, the unstable domain expands again. At subcritical velocity, instability is mainly caused by the electromagnetic suspension. The beam dissipates energy because of the Doppler waves. A significant change happens between $1.2v_{cr}$ and $1.3v_{cr}$, due to the increased energy from the anomalous Doppler waves, which radiate energy back to the vehicle. Beyond the critical velocity, the kinematic invariant intersects the dispersion graph in the third quadrant, where both the frequency and wavenumber are negative, leading to the presence of anomalous Doppler waves. These waves contribute to the wave-induced instability. As the velocity surpasses $1.3v_{cr}$, the stable domain enlarges once again.

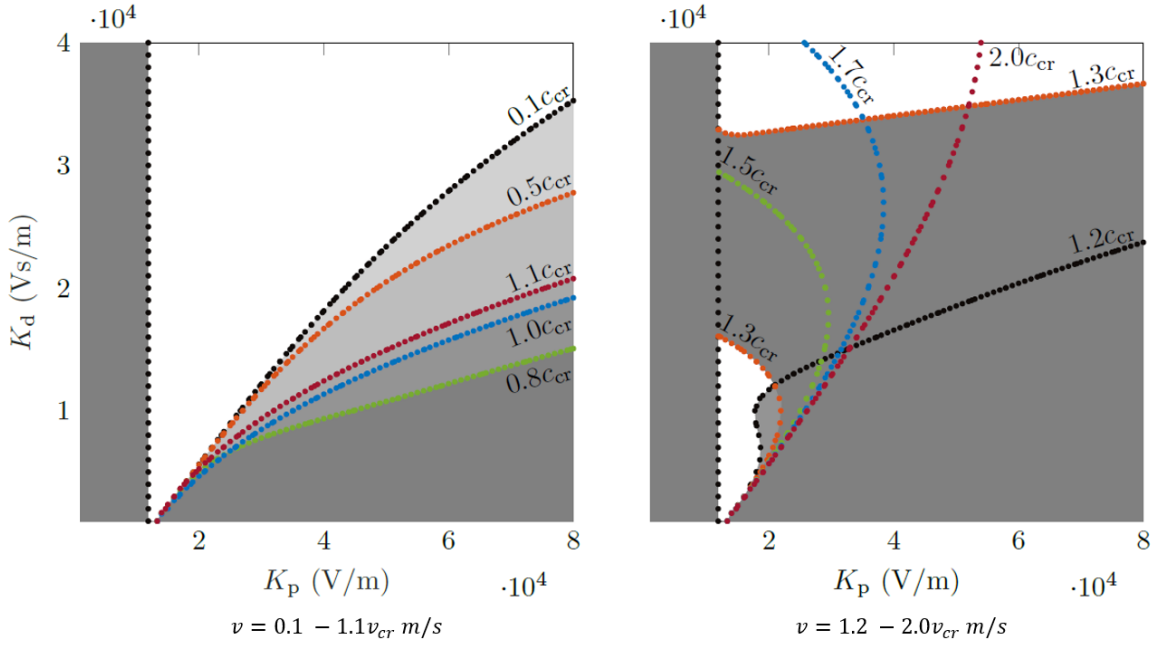

Figure 6.2: Stability planes against the control parameters for different velocities [6]. Instability happens in the grey areas. For the velocities, $1.5 - 2.0v_{cr}$ instability is to the right of the stability boundary.

6.1.2. 1.5 DOF Electromagnetically Suspended mass with Oscillating Base

First, the 1.5 DOF system without the constant aeroelastic force is discussed. The results for the 1.5 DOF system with an oscillating base are used as a comparison point for system 2 without the constant aeroelastic force. Paul et al. [27] derived analytical expressions for the coordinates of the centre and the size of the ellipse-shaped indentations in the stability boundary that represent the parametric resonance region. After eliminating I_{tr} from the equation of motion 4.16 (without the aeroelastic term), 4.17, and 4.18, the following simplified equation of motion is obtained:

$$2\left(CK_{\mathrm{p}}\sqrt{\frac{gM}{C}} - gMR\right)\Delta_{\mathrm{tr}} + 2CK_{\mathrm{d}}\sqrt{\frac{gM}{C}}\dot{\Delta}_{\mathrm{tr}} + z_{ss}MR\ddot{\Delta}_{\mathrm{tr}} + 2CM\dddot{\Delta}_{\mathrm{tr}} - A\cos(\Omega t)MR\ddot{\Delta}_{\mathrm{tr}} = 0 \quad (6.1)$$

Hill's determinant method is then used to obtain Hill's matrix, which is used to find the stability boundary. The air gap between the perturbed mass and the perturbed base, denoted as Δ_{tr} is expressed by the following complex Fourier series:

$$\Delta_{\mathsf{tr}} = \sum_{n=-\infty}^{\infty} d_n \exp(\mathrm{i}n\omega t); \Omega = k\omega; n, k \in \mathbb{Z} \tag{6.2}$$

The expressions for the centre of the ellipse (h_1, h_2), the major axis k_1, and the minor axis k_2 are:

$$\frac{(K_{\mathsf{p}} - h_1)^2}{k_1^2} + \frac{(K_{\mathsf{d}} - h_2)^2}{k_2^2} = 1 \tag{6.3}$$

$$\begin{aligned} h_1 &= \frac{R\left(2\sqrt{Cg^3M} + \sqrt{CgM} z_{ss} (\frac{\omega_1}{2})^2\right)}{2Cg} \\ h_2 &= \sqrt{\frac{CM}{g}} \left(\frac{\omega_1}{2}\right)^2 \\ k_1 &= \left(\frac{\omega_1}{2}\right)^2 k_2 \\ k_2 &= \sqrt{\frac{A^2 M R^2}{16Cg}} \end{aligned} \tag{6.4}$$

Furthermore, they also managed to derive analytical expressions for the 1.5 DOF system that is subjected to an aeroelastic force. In the paper, the expressions are obtained for an oscillating aeroelastic force. For now, the oscillating term is left out to focus on a constant aeroelastic force. The same procedure is taken as previously to obtain the expressions for the ellipse. Now, the aeroelastic term is included in equation 4.16. The expressions for the centre coordinates, major axis and minor axis are:

$$\begin{aligned} h_1 &= \frac{2\sqrt{Cg^3M^3}R + \sqrt{CgM^3} R z_{ss} (\frac{\omega_1}{2})^2 - 2\sqrt{C^3 g M} \mu (\frac{\omega_1}{2})^2}{2CgM} \\ h_2 &= \frac{\sqrt{CgM} R \left(2 z_{ss} \mu\right) + 4\sqrt{C^3 g M^3} (\frac{\omega_1}{2})^2}{4CgM} \\ k_1 &= \left(\frac{\omega_1}{2}\right) k_2 \\ k_2 &= \sqrt{\frac{A^2 R^2 \left(\mu^2 + M^2 (\frac{\omega_1}{2})^2\right)}{16CgM}} \end{aligned} \tag{6.5}$$

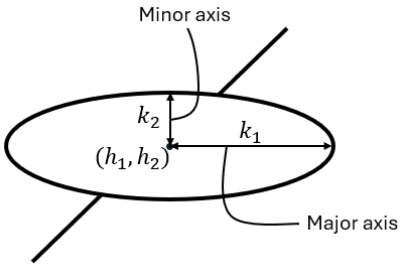

Figure 6.3: Definition of the major and minor axis

Appendix B and C illustrate the stability boundaries for the 1.5 DOF system and system 2.

6.2. Stability of a Continuously Supported Euler-Bernoulli Beam with an Electromagnetically Suspended Moving Mass and Constant Aeroelastic Force

In this section, the results for system 1 are illustrated and discussed. The eigenvalues of the system are presented, along with the stability planes corresponding to different velocities and situations. Finally, the time-history of a limit cycle is presented, showing the response of both the mass and the beam at the contact point. When it is mentioned that the system is stable or unstable, it only refers to the stability of the equilibrium point at which the system is linearised.

A comparison is made between the results from Fărăgău et al. [6] and those obtained in this thesis. Figure 6.4 illustrates the eigenvalues for the same combination of K_p and K_d used in the paper [6], showing how the system's stability state changes across varying velocities. The constant aeroelastic force varies with the velocities as described by equation 3.8. Similar to the findings of Fărăgău et al. [6], five eigenvalues are identified, of which two eigenvalues only appear in the range $v \approx 0.7 - 1.3v_{cr}$. These five eigenvalues consist of one real-valued eigenvalue and two pairs of complex-conjugate eigenvalues. Again for the stability analysis, only three eigenvalues determine the system's stability state. The real-valued eigenvalue remains constant across the velocity spectrum, as seen in the horizontal lines in Figure 6.4b. However, the complex-conjugate eigenvalues show significant variation across the velocity spectrum. Similar to the reference study [6], the real parts of the complex eigenvalues reach their lowest value at approximately $0.7v_{cr}$, where the system's vibrations decay the fastest, bringing the system back to its equilibrium. Below $0.7v_{cr}$, the decay rate increases, stabilising the system. Above $0.7v_{cr}$, the decay rate decreases. At approximately $1.3v_{cr}$, the real parts of the complex eigenvalues become positive, leading to a loss of stability through a supercritical Hopf bifurcation. As the velocity continues to increase, the real parts of the complex eigenvalues reach their highest point at approximately $1.4v_{cr}$, after which the vibrations start to decay again, while remaining unstable. Stability is not regained before $2.0v_{cr}$.

The aeroelastic force does not significantly change the eigenvalues across the velocity spectrum. However, the most important difference to highlight is the supercritical velocity at which the system re-stabilises. In this thesis, the system does not regain stability before $2.0v_{cr}$, while in Fărăgău et al.'s paper [6], the system stabilises again at approximately $1.7v_{cr}$. The eigenvalues at the lower velocities remain unchanged, indicating that the aeroelastic force has a greater impact at higher velocities. This conclusion is further supported by the stability planes.

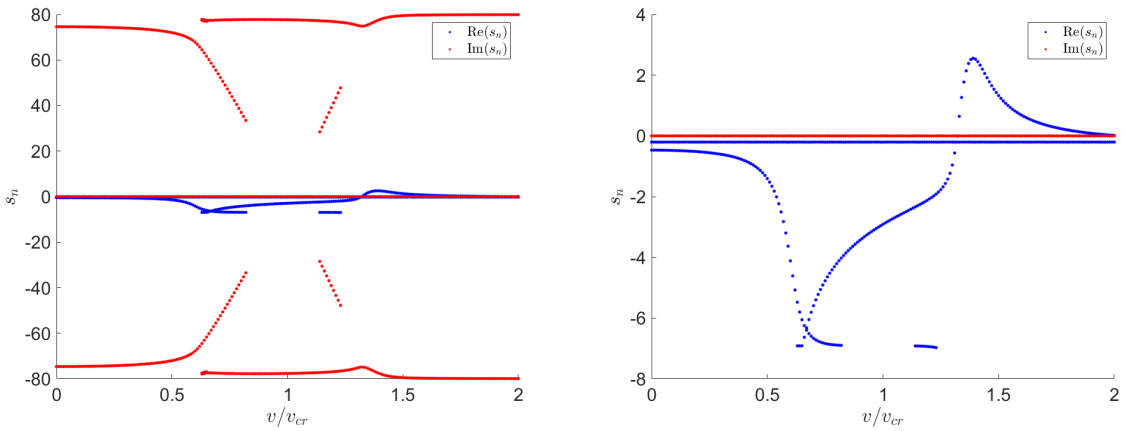

(a) Real part and Imaginary part

(b) Close up of the real part of the eigenvalues

Figure 6.4: The eigenvalues versus relative velocity of the vehicle. K_p = 2.0×10^4 V/m, K_d = 4.0×10^4 Vs/m. $\mu = \frac{1}{2}\rho_{air} A_v v \left(\frac{\partial C}{\partial \alpha}\right)_0$ and is calculated for every velocity.

Figure 6.5 illustrates the stability planes for the control parameters at different velocities. The grey domains indicate instability, while the white domains indicate stability. The unstable domains for velocities between $1.3 - 2.0v_{cr}$ are to the right of the stability boundary and are not shaded in grey to maintain a clear overview of the results. For all velocities, there is a minimum value for K_p below which the system is unstable for any value of K_d. The reason is that the controller cannot respond quickly enough to counteract the effect of gravity pulling the vehicle down. Figure 6.5a shows the stability planes for velocities up to $1.1v_{cr}$. As the velocity increases, the stable domain expands, having its smallest domain at $0.8v_{cr}$. Beyond $0.8v_{cr}$, the stable domain begins to shrink. At lower velocities, instability is mainly caused by the electromagnetic suspension and the constant aeroelastic force. The beam dynamics do not contribute to instability yet because the energy of the Doppler waves is greater than that of the anomalous Doppler waves. This ensures that the waves remain restrained within the guideway, preventing energy from radiating back into the vehicle and avoiding wave-induced instability.

When the velocity increases, as illustrated in Figure 6.5b, the stability planes show significant changes. The shifts in the stability zones become more pronounced with each velocity increment. At $1.2v_{cr}$, the stability boundary curves around 1.8×10^4 V/m, indicating that the system can either be stable or unstable depending on the value of K_d. The transition from $1.2v_{cr}$ to $1.3v_{cr}$ is especially noteworthy. The stable domain now becomes enclosed by the stability curve and the minimum value for K_p. As the velocity increases further, the stable domain expands again. The significant changes in the stability domains are primarily caused by the interaction between the moving vehicle and the guideway. When the velocity becomes supercritical, anomalous Doppler waves are present in the system. The energy of the anomalous Doppler waves increases, surpassing the energy of the Doppler waves. The anomalous Doppler waves feed back energy into the vehicle, amplifying the vehicle's oscillations, which expands the unstable domain.

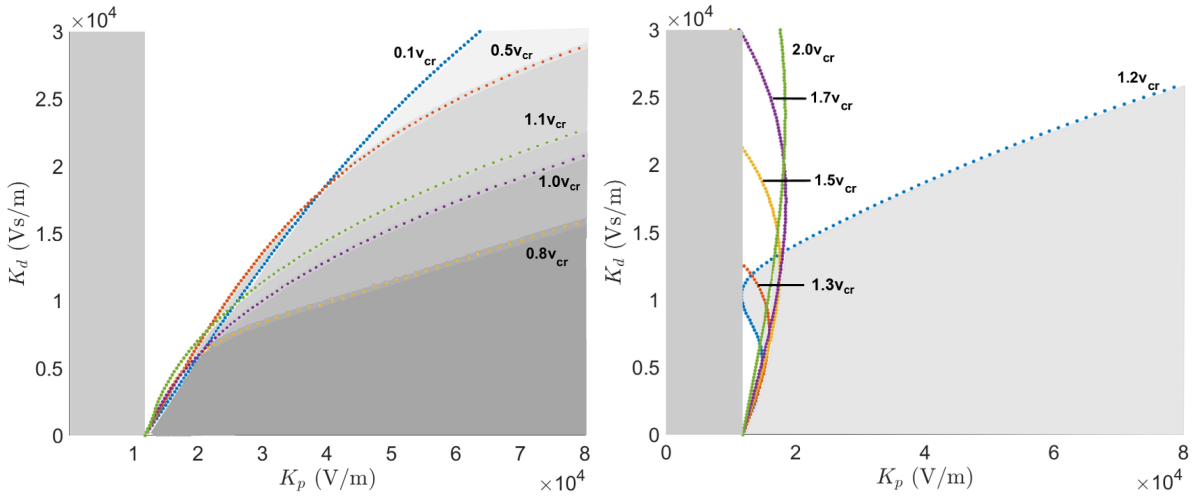

(a) $v = 0.1 - 1.1v_{cr}$ m/s **(b)** $v = 1.2 - 2.0v_{cr}$ m/s

Figure 6.5: Stability planes against the control parameters for different velocities. Instability is indicated with the grey areas. For the velocities, $1.5 - 2.0v_{cr}$ instability is to the right of the stability boundary.

Figures 6.6 and 6.7 illustrate the contributions of different instability mechanisms for the following cases: (1) solely electromagnetic instability, (2) electromagnetic instability and galloping, (3) electromagnetic instability combined with wave-induced instability, and finally (4) the combination of electromagnetic instability, wave-induced instability, and galloping.

Each scenario shows how the different instability mechanisms contribute to the system's overall stability. The electromagnetic suspension shows a specific unstable domain, which changes when combined with either the constant aeroelastic force or wave-induced effects. The constant aeroelastic force has a destabilising effect, which intensifies as the velocity increases, expanding the unstable domain. At subcritical velocities, the influence of the constant aeroelastic force differs, depending on

whether the beam dynamics are included or not. The constant aeroelastic force has a greater destabilising effect when only electromagnetic instability is considered, compared to when the wave-induced instability mechanism is also considered, as illustrated in Figure 6.7a. At $1.7v_{cr}$, the expansion of the unstable domain for both the case with solely electromagnetic instability and when the wave-induced instability is included becomes more comparable. For subcritical velocities, the wave-induced induced instability mechanism initially has a stabilising effect that counters the destabilising effect of the constant aeroelastic force. However, at supercritical velocities, both the wave-induced instability and the constant aeroelastic force are destabilising, amplifying one another and leading to a greater expansion of the unstable domain. The addition of the constant aeroelastic force does not result in qualitative changes in the stability boundaries compared to a system that only considers the electromagnetic and wave-induced instability mechanisms [6]. While the overall shape of the stability boundaries remains the same, quantitative differences are present.

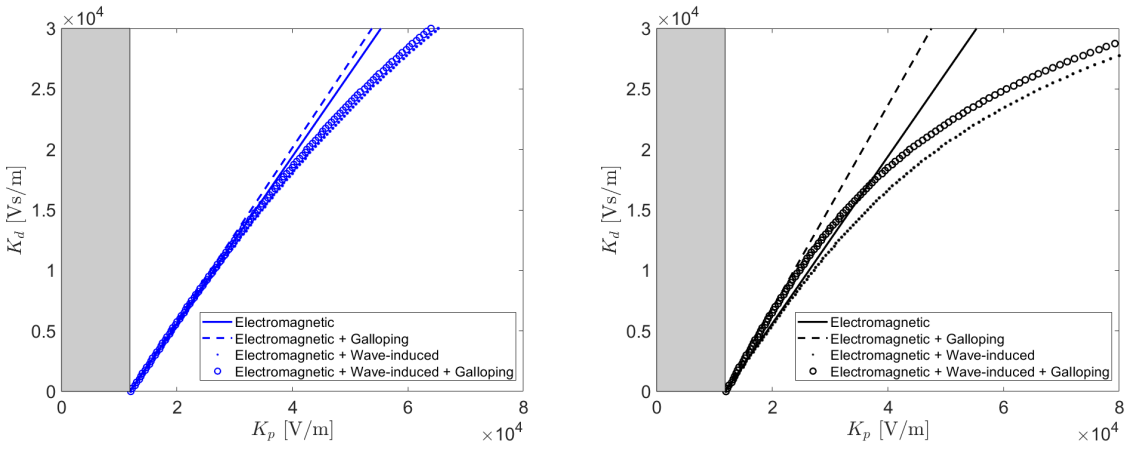

(a) $v = 0.1v_{cr}$ m/s **(b)** $v = 0.5v_{cr}$ m/s

Figure 6.6: Comparison of electromagnetic instability, wave-induced instability and aeroelastic force under different combination scenarios

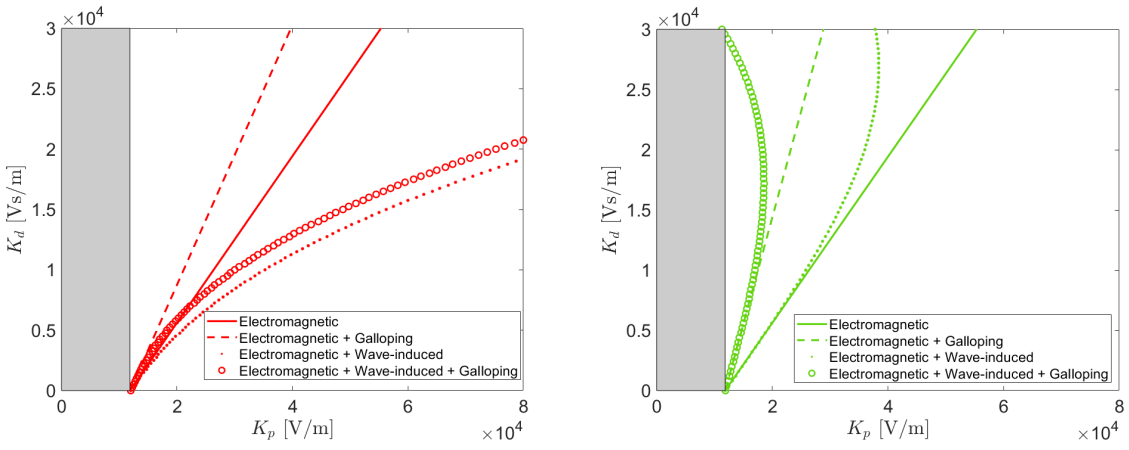

(a) $v = 1.0v_{cr}$ m/s **(b)** $v = 1.7v_{cr}$ m/s

Figure 6.7: Comparison of electromagnetic instability, wave-induced instability and aeroelastic force under different combination scenarios

The previous plots do not show any presence of limit cycles, but they are present. By selecting the control parameters within the limit cycle zone, the top panel of Figure 6.8 illustrates how the vehicle oscillates around the equilibrium point. The control parameters are chosen near the stability boundary. When K_p increases, the oscillations become larger, due to the stronger position feedback regulation.

Further increases in K_p eventually lead to a collision between the vehicle and the guideway. For the electromagnetic force, a collision with the guideway leads to an infinite force, as can be seen in equation 4.4, because of the air gap approaching zero, creating a division by an infinitely small value. The combination of control parameters and velocity used in Figure 6.8 is not the only situation where limit cycles occur because of the presence of electromagnetically induced instability [6].

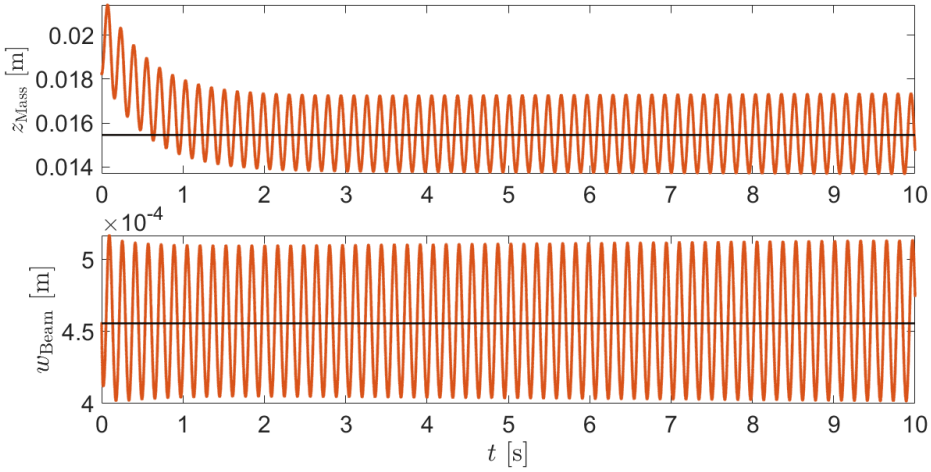

Figure 6.8: Time-history response of the mass and beam: $v = 1.0v_{cr}$ m/s, $K_p = 4.0 \times 10^4$ V/m, and $K_d = 2.0 \times 10^4$ Vs/m

Summary

In this section, the influence of the constant aeroelastic force on the stability of the Hyperloop is analysed when taking into account both the electromagnetic and wave-induced instability mechanisms. When comparing the eigenvalues of the systems with and without the constant aeroelastic force, no qualitative changes are observed. The eigenvalues remain nearly identical at subcritical velocities. The only noticeable difference is the velocity at which the system regains stability. For the system that excludes the constant aeroelastic force, stability is regained at approximately $1.7v_{cr}$ for the selected control parameters, while the system that included the constant aeroelastic force does not regain stability before $2.0v_{cr}$. This indicates that the destabilising effect of the aeroelastic force increases at higher velocities.

The stability planes further show the impact of the constant aeroelastic force as the velocity increases. At subcritical velocities, the wave-induced instability mechanism has a stabilising effect because of the Doppler waves, which do not radiate energy back into the vehicle. However, at supercritical velocities, the energy of the anomalous Doppler waves increases, radiating energy back into the vehicle and destabilising the system at the selected equilibrium point. Across all velocities, the constant aeroelastic force expands the unstable domain, as it continuously injects energy into the system, with the energy feedback increasing alongside the velocity. Although the constant aeroelastic force affects the stability quantitatively by expanding the unstable domain, it does not introduce qualitative changes to the overall shape of the stability boundaries, as compared to a system subjected solely to electromagnetic and wave-induced instability mechanisms.

Close to the stability boundary, limit cycles are present. The limit cycle zones cannot be visualised using the eigenvalue analysis. Due to the electromagnetic instability mechanism, limit cycles are present across all velocities and different combinations of K_p and K_d.

6.3. Irregular Euler-Bernoulli Beam with Continuous Support under an Electromagnetically Suspended Moving Mass

In this section, the results for system 2, excluding the constant aeroelastic force, are presented, to analyse the effect of the irregular guideway profile on the system's stability. The influence of the time-dependent parameters on the stability boundaries is highlighted by the appearance of ellipse-shaped indentation within the stability boundary, representing the regions of parametric resonance. Different scenarios are analysed to understand the effect of the time-dependent parameters on both the stability boundary and the size and position of the ellipses. When it is stated that the system is stable or unstable, it only refers to the stability of that equilibrium point at which the system is linearised.

6.3.1. Constant Wavelength with Changing Velocity

In reality, irregularities in the guideway are stochastic, with variations in the surface roughness wavelength and surface roughness amplitude, as highlighted by Chen et al. [2]. As noted in Chapter 4, the excitation frequency induced by the irregular guideway profile depends on both the vehicle's velocity and the surface roughness wavelength. In this section, the wavelength of the irregular guideway profile is fixed to examine the stability boundaries at different velocities. Fixing the wavelength gives insights into the stable and unstable control parameter combinations as the vehicle accelerates and decelerates. This allows for the selection of the control parameters that ensure stability throughout the vehicle's operation. Figure 6.9 illustrates the impact of the wavelength on the stability planes at various velocities, using approximately the same wavelength and amplitude reported by Chen et al. [2]. Appendix A further illustrates the stability planes for wavelengths of 20 m, 80 m, and 120 m.

The shape of the stability boundaries does not change across the varying wavelengths. However, the size and position of the ellipses change for different velocities and wavelengths. Notably, the stability boundary for $0.1v_{cr}$ disappears at higher wavelengths. For a wavelength of 20 m, the stability boundary is visible, and the corresponding ellipse is very small. Moreover, at supercritical velocities, there are no regions of parametric resonance for the chosen range of K_p and K_d for a wavelength of 20 m. The position of the ellipse depends on both the wavelength and the velocity. As the wavelength increases for a given velocity, the ellipse shifts downwards. As the velocity increases for a given wavelength, the ellipse shifts upwards. The shift of the ellipses is due to the changes in the excitation frequency. As the wavelength changes, the excitation frequency changes, which affects the dynamic behaviour of the system. The higher the excitation frequency, the higher the ellipse is along the stability boundary, resulting in a larger ellipse. On the contrary, the lower the excitation frequency, the lower the ellipse is along the stability boundary, resulting in a smaller ellipse. Increasing the velocity also increases the excitation frequency, amplifying the dynamic behaviour and enlarging the ellipse. A lower velocity has the opposite effect on the dynamic behaviour. As the velocity decreases, the excitation frequency also decreases. This leads to a smaller ellipse that shifts downward along the stability boundary.

The ellipses shift along the stability boundary because the natural frequency of the system varies along the boundary. Parametric resonance occurs when the excitation frequency is twice the natural frequency. This means that if the excitation frequency changes with variations in velocity or wavelength, the ellipse shifts to maintain this ratio.

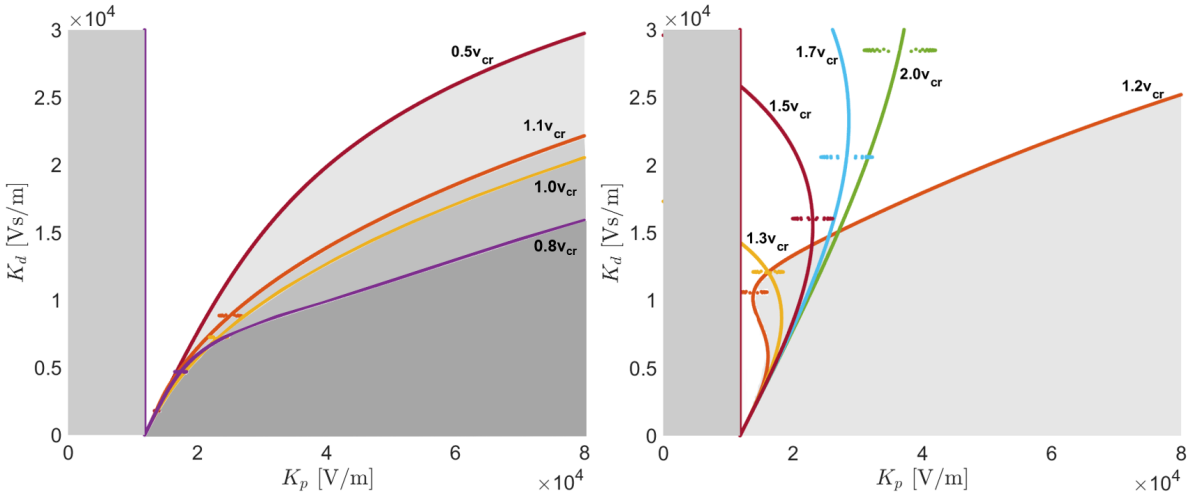

(a) $v = 0.1 - 1.1v_{cr}$ m/s, and $L = 100$ m

(b) $v = 1.2 - 2.0v_{cr}$ m/s, and $L = 100$ m

Figure 6.9: Stability planes for varying velocities and a constant wavelength of the surface roughness

To analyse the risk of parametric resonance, the range for control parameters used in maglev trains is employed. Based on the reviewed literature [9, 16, 26, 34, 38], it is observed that the PD controller is generally applied to the current rather than the voltage. Wu et al. [37] implements the controller to the voltage. In the references, the control parameters are given in units of A/m. For comparison, the control parameters are converted to V/m using the coil's resistance. The range for the control parameters is:

Control parameter	K_p [V/m]	K_d [Vs/m]
Range	$0 - 12 \times 10^4$	$0 - 0.4 \times 10^4$

Table 6.1: Range for the control parameters

Figure 6.10 illustrates the stability plane for a wavelength of 100 m and 120 m, focusing on the specified control parameter range. When considering the control parameter range found in the literature, only a limited domain remains where the system is stable. In the analysed stability planes, parametric resonance is absent for velocities of $1.2v_{cr}$ and above. However, parametric resonance may occur at velocities below $1.1v_{cr}$ as shown for the subcritical velocities. Because of the limited stable domain, parametric resonance can occur depending on the combination of K_p and K_d.

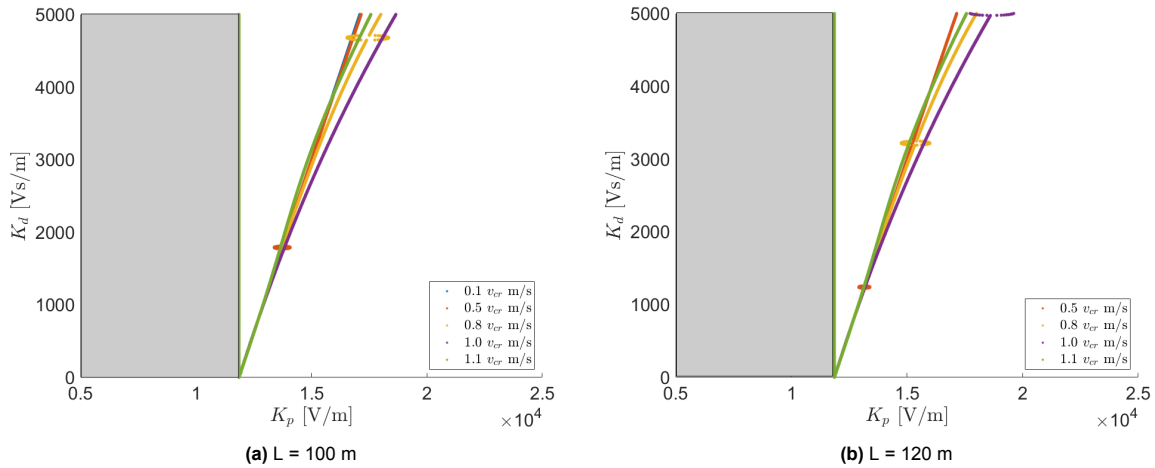

(a) L = 100 m **(b)** L = 120 m

Figure 6.10: Close up of the stability boundaries for the control parameter range as identified in the literature

6.3.2. Maintaining Constant Frequency by Adjusting Wavelength and Velocity

The figures in Appendix C illustrate the stability planes for a constant excitation frequency at different velocities and wavelengths. As the velocity changes, the wavelength must change accordingly to keep the excitation frequency constant at 80 rad/s. These results are compared to the response of the 1.5 DOF system with an oscillating base that is not subjected to an aeroelastic force. This comparison gives insights into the effects of the beam dynamics on the ellipses and whether the 1.5 DOF system is a suitable simplified model to approximate the beam model's behaviour. As discussed in Chapter 4, the base oscillations differ from the irregularities in the guideway. The amplitudes for the oscillations are adjusted so that the ellipses match in size, using an amplitude of 0.008 m for the irregular guideway profile and 0.004 m for the oscillating base.

The results show that the ellipses are located around 1.0×10^4 Vs/m, where the ellipses for system 2 are positioned slightly higher than those of the 1.5 DOF system. At a velocity of $1.7v_{cr}$, the horizontal position of the ellipses shows minimal differences. Comparing the results of the irregular guideway profile to the results in Figures 6.6 and 6.7, it is observed that the unstable domains in Figures C.1 and C.2 are slightly larger when irregularities are introduced. Figure 6.11 illustrates these positional differences between the stability boundaries at the location of the centre of the ellipse. In the results of Fărăgău et al. [6], no ellipses were observed, in this analysis the value of K_p at $K_d = 1.0 \times 10^4$ Vs/m is extracted to illustrate the horizontal shift of the stability boundary. Compared to the 1.5 DOF system, the stability boundary for Fărăgău et al.'s system aligns closer at subcritical and supercritical velocities than system 2. Around the critical velocity, there is an upward shift in K_p, which occurs approximately at the velocity where the real parts of the complex eigenvalues reach their lowest value. After this point, K_p starts to decrease until it reaches its minimum at approximately the velocity where the system becomes unstable, according to the eigenvalues.

The radiation of Doppler and anomalous Doppler waves causes the shifts around critical velocities. As the velocity increases, the energy of the Doppler waves increases, reducing the size of the unstable domain. In Figure 6.11 the shrinkage of the unstable domain is visualised with the upward shift of the K_p values. When the velocity becomes supercritical, the unstable domain expands due to the radiation of the anomalous Doppler waves. This causes the value of K_p to shift downwards. Finally, the analysis shows that the irregularities in the guideway contribute to the dynamic effects of the system. System 2 consistently has a larger unstable domain compared to the system described in the paper of Fărăgău et al. [6], indicating that the irregularities also increase the instability domain besides the addition of parametric resonance.

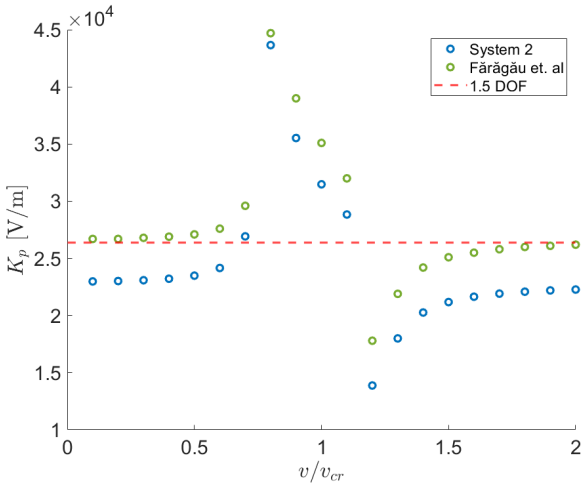

Figure 6.11: The values of K_p at the centre points for system 2 and 1.5 DOF system, at an excitation frequency of $\omega_1 = 80$ rad/s. For the system analysed by Fărăgău et al. K_p is extracted at $K_d = 1.0 \times 10^4$ Vs/m

The influence of the irregular guideway profile on the size of the ellipse is analysed by looking at the length of the major axis. Figure 6.12 illustrates the length of the major axis for system 2 without the constant aeroelastic force at different velocities, in comparison to the length of the major axis for the 1.5 DOF system without aeroelastic force. The results show that the size of the ellipse increases up to $0.7v_{cr}$ before it decreases. After a slight increase, the length of the major axis shrinks again at $1.3v_{cr}$, where it matches the length of the major axis for the 1.5 DOF system. Beyond $1.3v_{cr}$, the length of the major axis can be predicted using the analytical expression derived by Paul et al. [27], which is not the case for the subcritical velocities. At subcritical, the length of the major axis deviates from the analytical prediction. This behaviour can be related to the dynamic amplification factor (DAF) of the Euler-Bernoulli beam [28]. As the velocity increases, energy accumulates at the contact point, amplifying the dynamic response of the beam. This also affects the parametric instability, as shown in Figure 6.12. The length of the major axis was expected to increase until the critical velocity, however, this is not the case. After the critical velocity, the DAF decreases because the moving load travels faster than the energy, leaving the energy behind. As a result, the deflection of the beam at the contact point reduces, showing similarities to the behaviour observed with a rigid boundary. This is demonstrated by the fact that the analytical expression for the 1.5 DOF system provides an accurate approximation for the length of the major axis in system 2 at supercritical velocities.

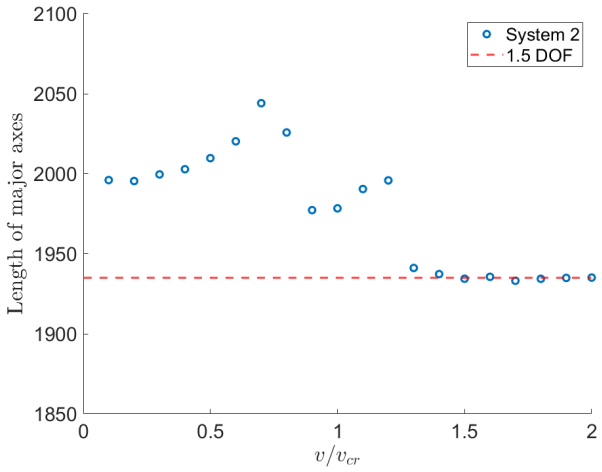

Figure 6.12: Length of the major axes at different velocities for $EI = 2.50 \times 10^{10}\ Nm^2$, at an excitation frequency of $\omega_1 = 80$ rad/s.

6.3.3. Changing Bending Stiffness

The bending stiffness is a critical parameter in the beam dynamics because it directly influences the natural frequency of the system. The ellipses that represent parametric resonance are positioned where the excitation frequency is twice the natural frequency. Figures 6.13 and 6.14 illustrate how altering the bending stiffness influences both the stability boundary and the ellipses' position. Changing the bending stiffness directly affects the critical velocity of the beam, as demonstrated in equation 2.28. When the bending stiffness changes while the velocity remains constant and independent of v_{cr}, the overall shape of the stability boundaries shifts. This behaviour is similar to that observed in Section 6.2, where the bending stiffness is fixed and the velocity is altered.

As the bending stiffness increases, the v/v_{cr} ratio decreases, making the stability boundaries behave more like those at subcritical velocities. Contrarily, when the bending stiffness decreases, the v/v_{cr} ratio increases, resulting in stability boundaries similar to those observed at supercritical velocities. As the bending stiffness changes, the ellipses shift horizontally due to the change in the overall shape of the stability boundary. A slight vertical shift is also observed, which is driven by the change in the natural frequency as the natural frequency of the system varies along the stability boundary.

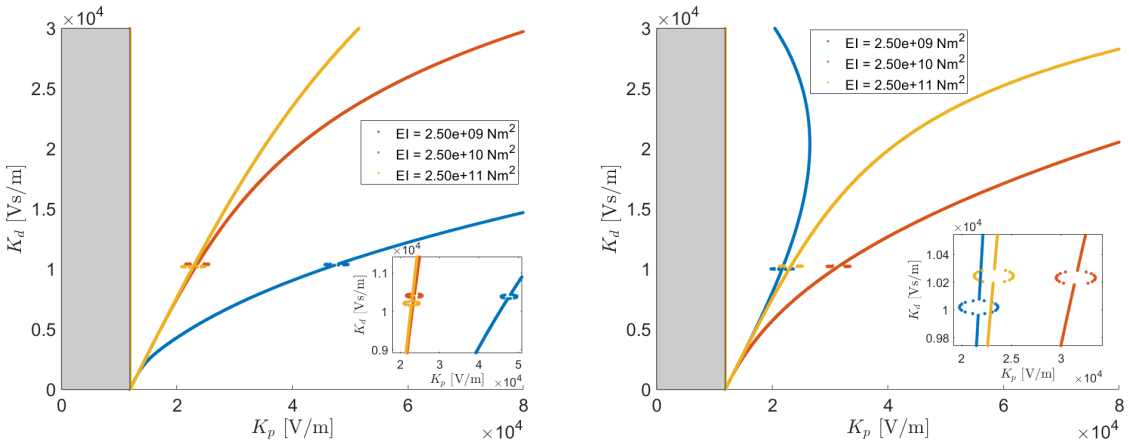

(a) $v = 536.6$ m/s **(b)** $v = 1073.2$ m/s

Figure 6.13: Stability planes for different bending stiffness values at a constant velocity

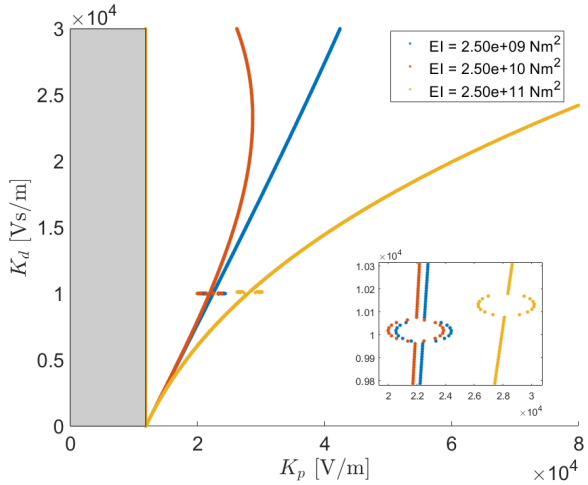

Figure 6.14: Stability planes for different bending stiffness values at a constant velocity, $v = 1824.4$ m/s

6.3.4. Changing the Surface Roughness Amplitude

The amplitude of the surface roughness is an essential parameter because of the high velocities and the small air gap of the Hyperloop system. The surface roughness amplitude influences the dynamic response, potentially leading to greater oscillations of the vehicle. These irregularities also influence the air gap distance, which is critical for the electromagnetic suspension. The influence of surface roughness amplitude is analysed to understand its effect on the stability boundaries and the ellipses.

Figure 6.15 illustrates the influence of the surface roughness amplitude on the stability plane and the parametric resonance ellipses. As the surface roughness amplitude increases, the size of the ellipse grows, increasing the chance of parametric resonance. Paul et al. [27] also observed that the size of the ellipse depends on the amplitude of the surface roughness. Furthermore, increasing the roughness amplitude expands the unstable domain, which was not observed in the 1.5 DOF system. Paul et al. [27] observed that the position of the stability boundary is independent of the oscillation amplitude. The beam dynamics makes the position of the stability boundary dependent on the surface roughness amplitude. This behaviour can either be due to reduced energy dissipation of the beam or due to the increased energy input from the electromagnetic suspension reacting to the irregularities. Because of the high velocities and the small air gap in the Hyperloop system, it is necessary to minimise the irregularities in the guideway. Large roughness amplitudes are undesired because they expand the unstable domain and increase the change of parametric resonance. In Section 6.3.1, it is stated that the stable domain for the control parameter combinations in maglev trains is already narrow. The roughness amplitude can potentially further narrow the already limited stable domain.

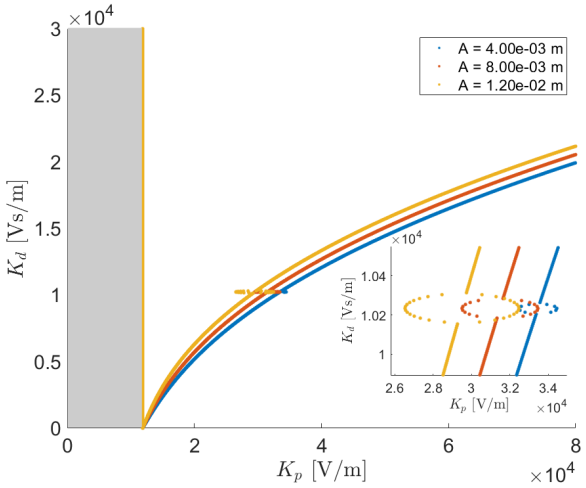

Figure 6.15: Stability plane for different surface roughness amplitudes at $v = 1.0v_{cr}$ m/s

The ellipses shift horizontally as the overall stability boundary shifts, but their vertical position remains constant because of the maintained ratio $\frac{\omega}{\omega_1} = \frac{1}{2}$. The excitation frequency and natural frequency remain unchanged when the roughness amplitude changes. Figure 6.16 illustrates the position of the centre of the ellipse at critical velocity for system 2, compared to the ellipse of the 1.5 DOF system without the aeroelastic force, as well as the value of K_p at $K_d = 1.0 \times 10^4$ Vs/m from Fărăgău et al.'s paper. The centre points of the ellipses for system 2 are located between the results from the other two systems. As the roughness amplitude approaches zero, the position of the stability boundary for system 2 aligns with the results from Fărăgău et al. [6]. The horizontal position of the ellipse, against the surface roughness amplitude, now depends on the flexibility of the beam. The ellipse of the 1.5 DOF system is positioned closer to the y-axis compared to system 2 because the Doppler waves dissipate more energy in the beam, causing the stability boundary to bend to the right, which results in the horizontal shift of the ellipse.

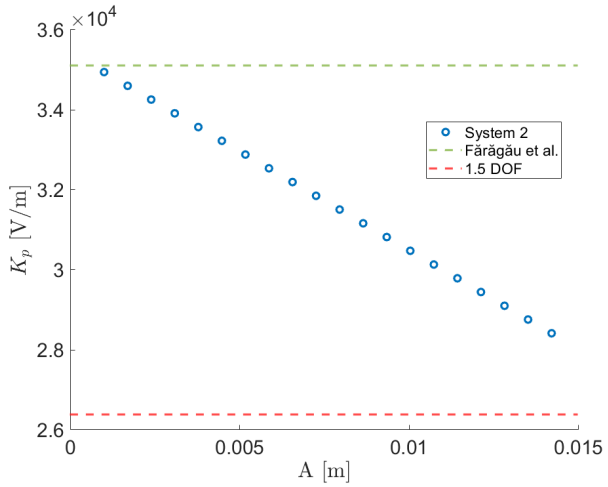

Figure 6.16: Values of K_p at the centre points for system 2 and 1.5 DOF system as a function of the amplitude, at an excitation frequency of $\omega_1 = 80$ rad/s. For the system analysed by Fărăgău et al., K_p is extracted at $K_d = 1.0 \times 10^4$ Vs/m with $v = 1.0 v_{cr}$

Figure 6.17 illustrates that the length of the major axis for system 2 is almost identical to that of the 1.5 DOF system. The relationship between the length of the major axis and the surface roughness amplitude is minimally affected by the flexibility of the beam. The analytical expression for the length of the major axis derived for the 1.5 DOF system provides an accurate approximation for the length of the major axis of the ellipse for system 2 when the aeroelastic force is excluded. This makes the 1.5 DOF system a valuable system for estimating the ellipse size of more complicated systems, that include the beam dynamics.

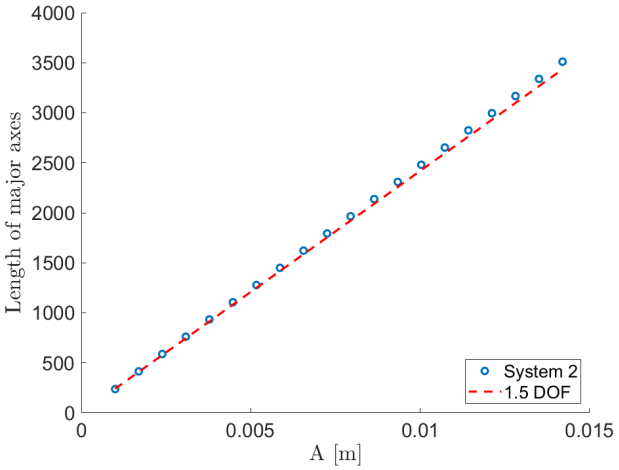

Figure 6.17: Length of the major axis as a function of the oscillation amplitude, at an excitation frequency of $\omega_1 = 80$ rad/s.

Summary

A comparison is conducted between the irregular Euler-Bernoulli beam without an aeroelastic force (system 2), the 1.5 DOF electromagnetically suspended mass system with an oscillating base (without an aeroelastic force) at a frequency matching that of system 2, and the system discussed by Fărăgău et al. For the velocities up to $0.7v_{cr}$ and beyond $1.5v_{cr}$, the stability boundary at 1.0×10^4 Vs/m for the system discussed by Fărăgău et al. [6] aligns with the analytical predictions for the 1.5 DOF system's centre point. However, this does not hold for system 2. While system 2 and the system discussed by Fărăgău et al. [6] do not show qualitative differences, quantitative differences are present, indicating that the irregular guideway profile not only expands the unstable domain but also introduces ellipse-shaped indentations in the stability boundary that indicate the parametric resonance regions.

Further comparisons between the major axis lengths in system 2 and the 1.5 DOF system show that the length of the major for system 2 increases as the velocity increases. This behaviour is explained by looking at the dynamic amplification factor (DAF) of the Euler-Bernoulli beam. As the velocity increases, the dynamic response at the contact point increases due to the accumulation of energy. At supercritical velocities, the vehicle moves faster than the rate at which the energy propagates, leaving behind the energy. As a result, the deflection at the contact point reduces, showing similar behaviours to that of a rigid boundary. At velocities of $1.3v_{cr}$ and above, the length of the major axis can be accurately approximated using the analytical expressions for the 1.5 DOF system.

Bending stiffness directly changes the critical velocity. To analyse this effect, the bending stiffness was varied while keeping the velocity of the vehicle constant and independent of the critical velocity. An increase in the bending stiffness raises the critical velocity, reducing the v/v_{cr} ratio. This reduction makes the stability boundaries more comparable to those observed at subcritical velocities when the bending stiffness is maintained constant. Conversely, as the bending stiffness decreases, the critical velocity also decreases. The v/v_{cr} ratio increases, making the stability boundaries resemble those found at supercritical velocities for a constant bending stiffness. Vertical shifts in the ellipses are observed due to the variations of the natural frequency along the stability boundary. Since the bending stiffness directly influences the natural frequency, adjustments of the bending stiffness cause the ellipses to shift vertically.

Increasing the surface roughness amplitude not only enlarges the ellipses but also expands the unstable domain. This can either be due to the reduced energy dissipation by the beam or the altered response of the electromagnetic suspension to the irregular guideway profile. This can increase the electromagnetic energy input, leading to the enlargement of the unstable domain. As the surface roughness amplitude approaches zero, the stability boundary at $K_d = 1.0 \times 10^4$ Vs/m aligns with the position found by Fărăgău et al. [6] at a velocity of $1.0v_{cr}$. Additionally, comparing the length of the major axis of system 2 and the 1.5 DOF system shows that the analytical expression for the 1.5 DOF system provides an accurate approximation of the length of the major for system 2 when the aeroelastic force is excluded.

For the control parameter combinations commonly used in maglev trains, the remaining stable domain is relatively limited. Given this constraint, the surface roughness amplitude becomes an important parameter. As the roughness amplitude increases, it both enlarges the ellipse size and expands the unstable domain. This increases the chance of instability and parametric resonance.

6.4. Irregular Euler-Bernoulli Beam with Continuous Support under an Electromagnetically Suspended Moving Mass and Constant Aeroelastic Force

Figures 6.18 and 6.19 illustrate the stability planes for different velocities at a constant roughness amplitude and wavelength for system 2. Similar behaviours are observed in sections 6.2 and 6.3 at velocities below and up to $1.1v_{cr}$. As seen in the previous systems, $0.8v_{cr}$ has the smallest unstable domain, after which it increases for $1.0v_{cr}$ and $1.1v_{cr}$. At supercritical velocities, the anomalous Doppler waves become dominant, feeding energy back into the vehicle, and further expanding the unstable domains. The stability planes change significantly for velocities up to and beyond $1.2v_{cr}$. Notably, the stable domain for $2.0v_{cr}$ is absent in the figures. At $1.3v_{cr}$, $1.5v_{cr}$, and $1.7v_{cr}$ only a narrow stable domain is present. Both the irregular guideway profile and the constant aeroelastic force contribute as destabilising factors, amplifying the instability more than in the previous systems.

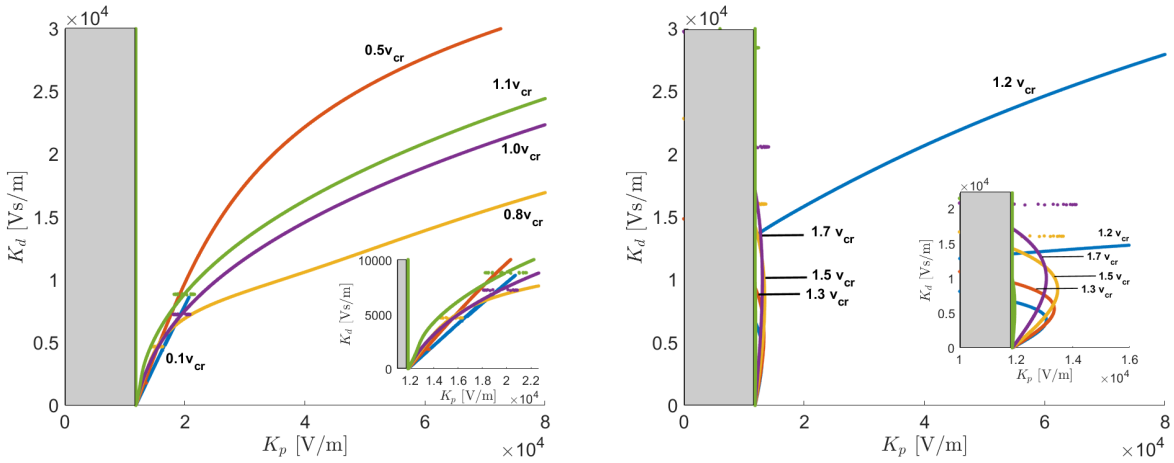

(a) $v = 0.1v_{cr} - 1.1v_{cr}$ m/s **(b)** $v = 1.2v_{cr} - 2.0v_{cr}$ m/s

Figure 6.18: Stability planes for different velocities at L = 100 m

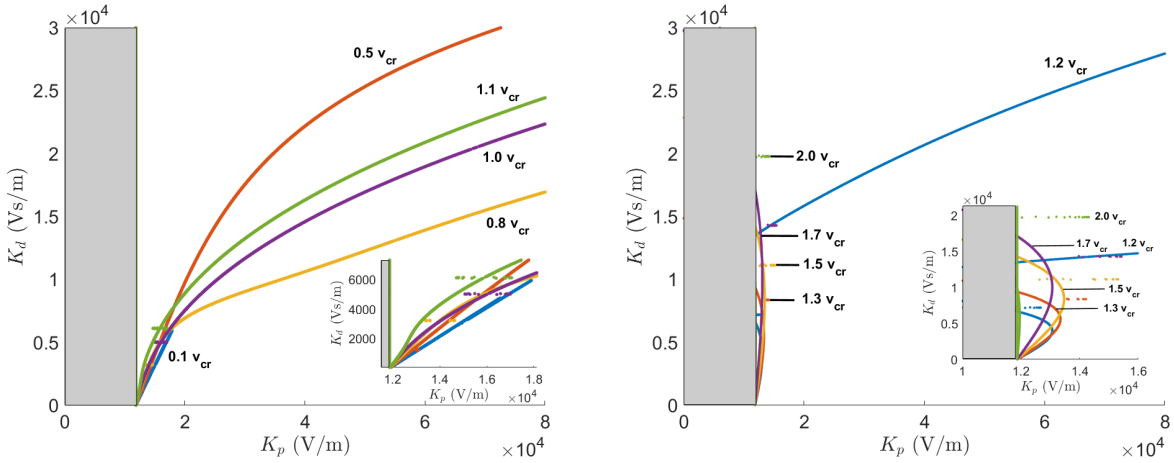

(a) $v = 0.1v_{cr} - 1.1v_{cr}$ m/s **(b)** $v = 1.2v_{cr} - 2.0v_{cr}$ m/s

Figure 6.19: Stability planes for different velocities at L = 120 m

Figures 6.20 and 6.21 illustrate the effects of the constant aeroelastic force by comparing the results with those in section 6.3, where the system is not subjected to a constant aeroelastic force. The excitation frequency is kept constant at 80 rad/s to solely analyse the aeroelastic effects. As expected, the results show that the constant aeroelastic force has a destabilising effect, with the unstable domain expanding as the velocity increases. The influence of the constant aeroelastic force becomes more pronounced at higher velocities, contributing more to the overall stability of the system.

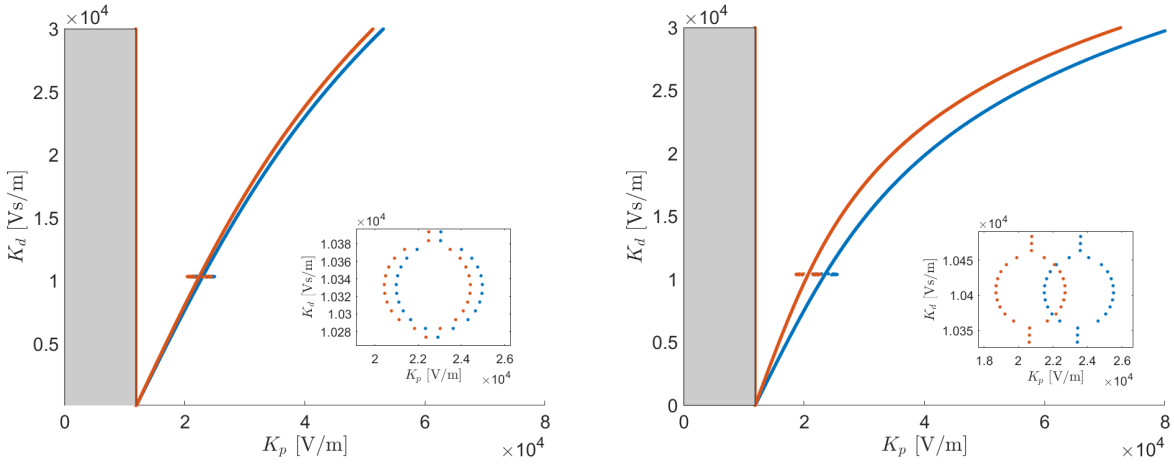

(a) $v = 0.1v_{cr}$ m/s **(b)** $v = 0.5v_{cr}$ m/s

Figure 6.20: Comparison of stability planes for system 2 with and without the aeroelastic force. The blue line is the stability plane without the constant aeroelastic force. The orange line is the stability plane with the constant aeroelastic force

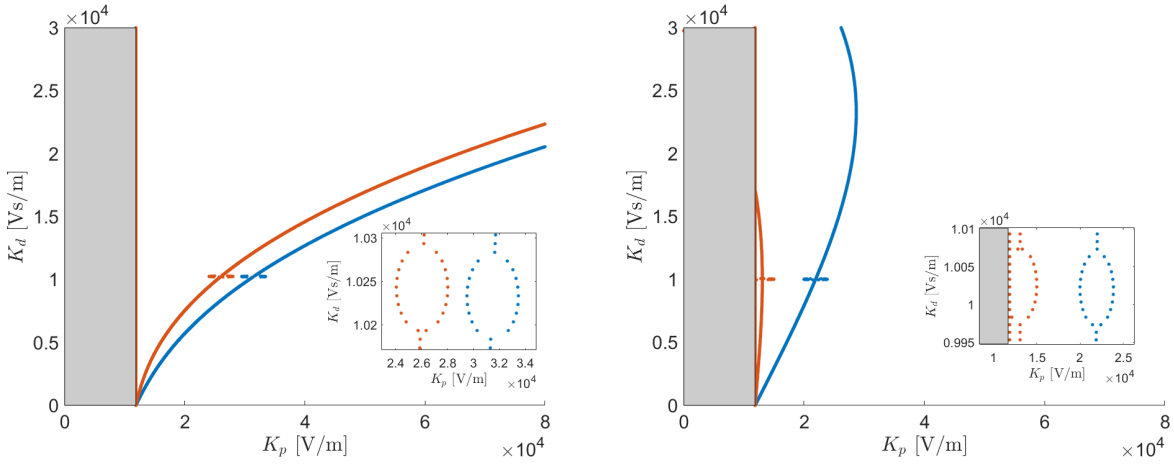

(a) $v = 1.0v_{cr}$ m/s **(b)** $v = 1.7v_{cr}$ m/s

Figure 6.21: Comparison of system 2 stability planes for with and without the aeroelastic force. The blue line is the stability plane without the constant aeroelastic force. The orange line is the stability plane with the constant aeroelastic force

Figures 6.21a and 6.21b show the minimal vertical movement of the ellipses, while the horizontal movement is visualised in Figure 6.22. This Figure compares system 2 with and without the constant aeroelastic force to the 1.5 DOF system with an oscillating base and a constant aeroelastic force. The ellipses are nearly aligned at a velocity of $v = 0.1v_{cr}$. This indicates that the constant aeroelastic force has little impact, aligning with the stability planes where the stability boundaries almost overlap. As the velocity increases, the distance between the stability boundaries increases gradually, as observed in the previous stability planes. System 2 shows a trend similar to that of the 1.5 DOF system at both subcritical and supercritical velocities.

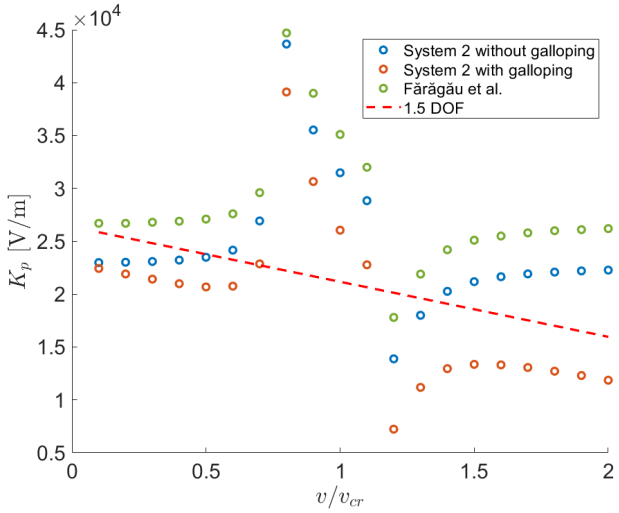

Figure 6.22: Value of K_p at the centre point for the 1.5 DOF system with a constant aeroelastic force, and for system 2 both with and without the constant aeroelastic force, at an excitation frequency of $\omega_1 = 80$ rad/s. For the system analysed by Fărăgău et al., K_p is extracted at $K_d = 1.0 \times 10^4$ Vs/m.

Regarding the size of the ellipses, no significant differences are observed with the addition of the constant aeroelastic force. Figure 6.23 shows that the lengths of the major axes are nearly identical, apart from some minor differences. The same discussion holds here as for Section 6.3.

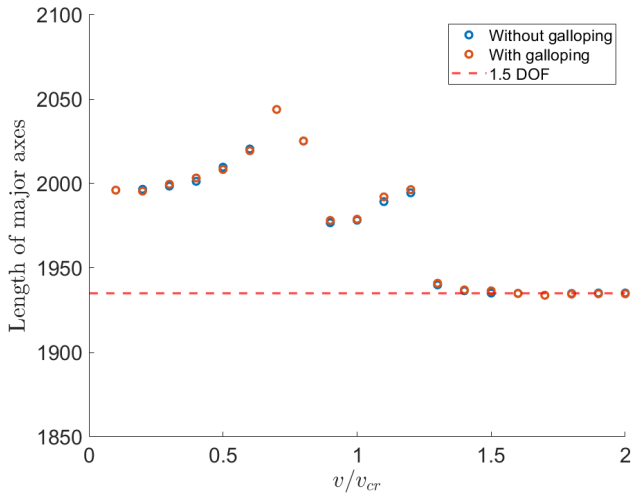

Figure 6.23: The length of the major axis with and without the constant aeroelastic force

Summary

The addition of the constant aeroelastic force to the system with the irregularities in the guideway leads to quantitative changes in the stability boundary but no qualitative changes are introduced. The most noticeable difference is the significant expansion of the unstable domains at supercritical velocities. Both the constant aeroelastic force and parametric instability are destabilising factors, causing the size of the stable domain to reduce significantly. At a velocity of $2.0v_{cr}$, no stable domain remains within the selected range for K_p and K_d. This highlights the combined destabilising effect of the constant aeroelastic force and parametric instability.

Notably, the addition of the constant aeroelastic force does not influence the size of the ellipse compared to the system without the constant aeroelastic force.

6.5. Electromagnetically Suspended Mass on an Oscillating Base Under a Varying Aeroelastic Force

In this chapter, the results for system 3 are presented. First, the Floquet eigenvalues are provided and analysed to understand the system's stability behaviour. Furthermore, the stability plane is illustrated, focusing on examining the impact of the modulated aeroelastic force.

Figure 6.24 illustrates the Floquet eigenvalues for the system with the oscillating boundary and a modulated aeroelastic force, along the orange line in figure 6.25. The system has three eigenvalues: one real-valued and two complex-valued eigenvalues. At $K_p \approx 1.2 \times 10^4$ V/m, the real parts of the Floquet eigenvalues are negative, indicating stability. However, the value of K_p at which the system regains stability depends on the aeroelastic parameter μ_2.

The smaller the value of μ_2, the lower the value for K_p at which the system becomes unstable again. For μ_2 = 0, instability occurs at $K_p \approx 2.1 \times 10^4$ V/m, while for μ_2 = 2000, instability occurs at $K_p \approx 2.3 \times 10^4$ V/m. Another key observation is the distance between the Floquet eigenvalues as μ_2 varies. At μ_2 = 0, the real parts of the complex Floquet eigenvalues are furthest apart. As μ_2 increases, the real parts converge until they nearly overlap, transitioning into complex-conjugates. When μ_2 increases beyond μ_1, the real parts of the eigenvalues deviate again. The transition between stability and instability, as well as the distance between the real parts of the Floquet eigenvalues, can be seen in the stability planes.

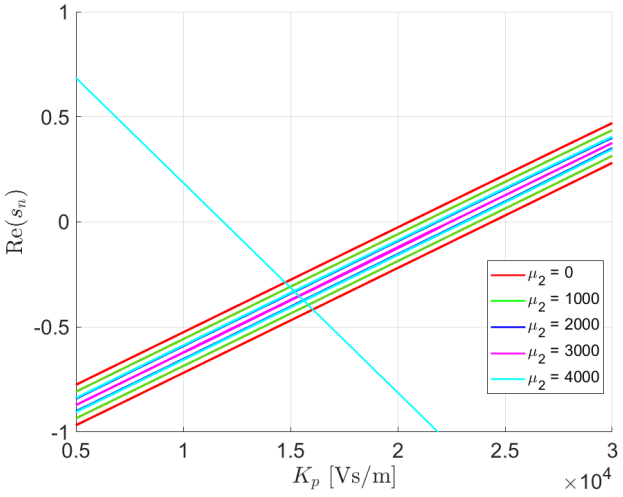

Figure 6.24: Real part of the Floquet eigenvalues for the oscillating base for various aeroelastic coefficients μ_2, with $\mu_1 = 3000$, evaluated at different values for K_p and $K_d = 1.02 \times 10^4$ Vs/m

In Chapter 5, it was explained that parametric instability can result from time-dependent parameters within the system. The ellipse-shaped indentation in the stability plane signifies regions where the excitation frequency is twice the system's natural frequency, potentially leading to parametric instability. The black line in Figure 6.25 represents the stability boundary for system 3 without the aeroelastic force, where only the oscillating base with the electromagnetic suspension is considered. Both the size and position of the ellipse depend on the aeroelastic coefficients. The stability boundary shifts as a result of the constant aeroelastic parameter, μ_1. Parameter μ_2 influences the size of the ellipse. When μ_2 is zero, the ellipse maintains its original size, as the oscillating boundary only causes parametric instability. As μ_2 increases, the ellipse shrinks until it disappears. Looking back at the Floquet eigenvalues at μ_2 = 3000, it is observed that the real parts of the Floquet eigenvalues are slightly separated, indicating that an ellipse is still present. At μ_2 = 4000, the ellipse appears again. However, this is unlikely to happen because the aeroelastic force cannot take away energy from the system.

The observation made in the real parts of the complex eigenvalues can be connected to the stability planes. The distance between the real parts of the complex Floquet eigenvalues corresponds to the width of the ellipse at the same value for K_d. This width illustrates the range of K_p values where parametric resonance can occur. The region extending from the vertical boundary to the edge of the ellipse represents the range where the real parts of all Floquet eigenvalues are negative, indicating stability.

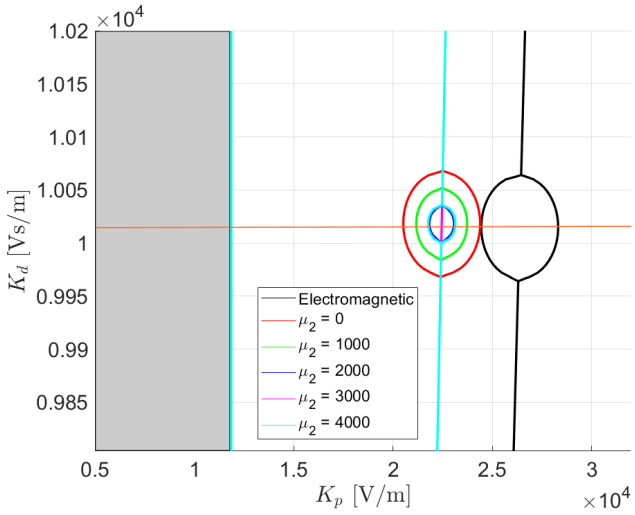

Figure 6.25: Stability plane for the control parameters for different values of the aeroelastic coefficient, μ_2

Figure 6.26 illustrates the time-history response of system 3 for a specific combination of K_p and K_d positioned to the left of the green ellipse in Figure 6.25. The amplitude of the oscillations varies over time, with periods of high and low amplitudes. The variations are influenced by the gravitational pull and the movement of the base. These factors can either amplify or dampen the oscillations depending on their relative phase.

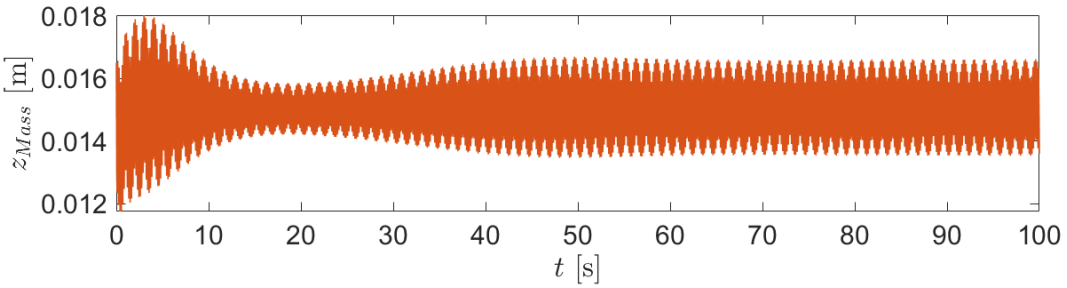

Figure 6.26: Time-history response for system 2 with parameters μ_1 = 3000, μ_2 = 1000, $K_p = 2.1 \times 10^4$ V/m and $K_d = 1.0 \times 10^4$ Vs/m

Summary

The 1.5 DOF system without an oscillating base or modulated aeroelastic force has three eigenvalues, with two of them being complex-conjugates. When the oscillating base is introduced, the two complex-conjugate eigenvalues values lose their symmetry. The addition of the modulated aeroelastic force caused a shift in the real parts of these complex eigenvalues. As the aeroelastic parameter μ_2 increases the real parts of the complex eigenvalues shift towards each other until they overlap. However, increasing μ_2 further shows that the eigenvalues deviate again.

The stability boundaries reveal that μ_1 has an impact on the position of the stability domain, while μ_2 impacts the size of the ellipse-shaped indentations in the stability boundary. As μ_2 increases the ellipse shrinks until it almost vanishes. When μ_2 increases further, the ellipse expands again. This observation is similar to what happens with the distance between the real parts of the complex eigenvalues.

When the control parameters are selected close to the stability boundary, the time response shows the presence of a limit cycle, with a fluctuating oscillation amplitude over time. This behaviour depends on the relative phase between the oscillating boundary and the oscillations of the mass, with their interaction either amplifying or dampening one another.

7

Conclusion

This thesis investigates the instability of the Hyperloop system through different models. Five research questions are addressed to clarify the influence of aeroelastic forces, electromagnetic suspension, wave-induced effects, and guideway profile irregularities on the system's stability. Through the models, this thesis provides insights into how each factor, both individually and in combination, influences the stability of the Hyperloop system.

> How does the aerodynamic instability mechanism change the stability of the Hyperloop system, when initially only considering electromagnetic and wave-induced instability mechanisms?

Compared to the results obtained by Fărăgău et al. [6], no qualitative differences in the stability boundaries are observed, however, quantitative differences are present. The system still loses stability through a supercritical Hopf bifurcation. The constant aeroelastic force has a destabilising effect on the system across all velocities, and its effect intensifies as the velocity increases. The severity of the destabilising effect also depends on the system parameters, such as the bending stiffness.

> How does the irregular guideway profile impact the stability of the Hyperloop system when considering the electromagnetic and wave-induced instability mechanisms?

The irregular guideway profile introduced ellipse-shaped indentation within the stability boundary, indicating regions of parametric resonance. These ellipses are located where the excitation frequency is twice the natural frequency. As the natural frequency varies along the stability boundary, the ellipses may shift accordingly, driven by changes in the excitation frequency, among other factors. Furthermore, the amplitude of the surface roughness expands the unstable domain and enlarges the ellipses.

> How does the aerodynamic instability mechanism impact the stability of the Hyperloop system when considering the effects of an irregular guideway profile along with electromagnetic and wave-induced instability mechanisms?

Introducing a constant aeroelastic force expands the unstable domain, with its destabilising effect increasing as the velocity increases, aligning with the previous findings. When the constant aeroelastic force is combined with the effects of the irregular guideway profile, the unstable domain expands significantly, particularly at supercritical velocities. Both the constant aeroelastic force and the irregular guideway profile contribute to the destabilisation of the system, where the irregular guideway profile also introduces the risk of parametric instability. The constant aeroelastic force does not affect the size of the ellipse-shaped indentation within the stability boundary. This feature remains solely influenced by the guideway's irregular profile and the beam's bending stiffness.

How does a modulated aeroelastic force influence the parametric instability of a system subjected to an oscillating boundary?

The aeroelastic force now consists of both a constant and oscillating part, affecting the size of the ellipse-shaped region, while also enlarging the overall unstable domain. Specifically, the constant term influences the size of the unstable domain, while the modulated aeroelastic part influences the size of the ellipse. Without the aeroelastic force, parametric instability is induced solely by the oscillating base. However, adding the modulated aeroelastic force shows an interplay between the aeroelastic force and the oscillating base within the parametric resonance region. The modulated aeroelastic force can mitigate the parametric instability caused by the oscillating base, potentially eliminating it. The modulated aeroelastic force and oscillating base can also work together and enlarge the ellipse-shaped indentation in the stability boundary. Furthermore, limit cycles are present near the stability boundary. These limit cycles are characterised by an amplitude that varies over time, influenced by the relative phase between the oscillating boundary and the oscillations of the mass.

To what extent is the electromagnetically suspended mass system with an oscillating base capable of approximating more complicated systems that include beam dynamics and an irregular guideway profile subjected to a constant aeroelastic force?

Paul et al. [27] derived analytical expressions to approximate the position and size of the ellipse-shaped indentation within the stability boundary. When the frequency of the oscillating base is equal to the excitation frequency from the guideway's irregular profile, the results show that the analytical expressions do not approximate the position of the ellipses across all velocities, and therefore also the stability boundary. However, for velocities beyond $1.3v_{cr}$, the analytical approximations provide an accurate approximation.

When beam dynamics are included, the position of the stability boundary becomes dependent on the amplitude of the irregular profile, which also affects the position of the ellipse-shaped indentation. This is not the case for the 1.5 DOF electromagnetically suspended mass system. Despite the added complexity, the size of the ellipse, as a function of the oscillation amplitude, can be accurately approximated using the analytical expressions.

Final Statement on Parametric Instability

The interaction between the guideway's irregular profile and the aeroelastic force significantly reduces the stable domain, limiting the range of stable control parameters. Within this limited stable range, the parametric resonance regions only appear at subcritical velocities and are relatively small compared to the stable control parameter domain. The surface roughness amplitude is crucial in defining both the stable domain and the extent of parametric resonance. A larger surface roughness amplitude increases the risk of instability and parametric resonance. To reduce the likelihood of instability and parametric resonance, the guideway should be manufactured as smoothly as possible.

8

Recommendations for Further Research

To expand this thesis and develop a more accurate model of the Hyperloop system, the following recommendations are proposed:

1. The resultant of the drag and lift forces is angle-dependent, represented by the coefficient $\left(\frac{dC_z}{d\alpha}\right)_0$, which is now assumed to be -1. However, both drag and lift forces are influenced by the pressure inside the tube. To determine this relationship, a finite element model (FEM) model of the Hyperloop vehicle within a pressure-regulated tube can be developed. By linking the drag and lift coefficients to the pressure, the internal pressure could be optimised to maintain high velocities without changing the dynamics of the system. This allows for the optimisation of the vacuum pumps to save as much energy as possible.

2. An energy analysis can be performed to visualise the contribution of the different instability mechanisms to the overall instability across the different velocities. By identifying the biggest contributor to the instability, specific mitigation methods can be implemented to reduce the impact of that instability mechanism.

3. In this thesis, the tube and guideway are modelled as a beam. However, the dynamic behaviour of the tube is not captured with a beam model. Considering the tube and guideway separately, where the guideway is attached to the tube through springs, would be a more realistic model. Additionally, modelling the guideway as a Timoshenko beam instead of the Euler-Bernoulli beam would capture the shear deformation and rotation inertia, proving more accurate results. To approximate reality further, periodic ring stiffeners could be placed in the tube by varying the stiffness at specified locations.

4. In this thesis, the foundation is modelled as a continuous viscoelastic foundation. However, the tube is supported periodically by piles. Replacing the continuous viscoelastic foundation with periodic springs introduces the possibility of parametric instability. Examining the interaction between the irregular guideway profile and the periodic supports could reveal interesting effects on the stability boundaries and the ellipse-shaped indentations. The next step could be to combine the periodic supports with the model described in the third point.

5. In reality, irregularities are random and cannot be represented by a cosine function. To achieve a more accurate model, a random signal could be implemented for these irregularities. The influence of random surface roughness on the region of parametric instability can be compared to the results of the cosine function to understand the effect of more realistic imperfections.

6. The final recommendation is to investigate the effects of a modulated aeroelastic force in combination with wave-induced instability, electromagnetic instability mechanisms, and profile irregularities in the guideway. This analysis would provide insight into how these combined factors influence the instability and the regions of parametric resonance.

References

[1] K. J. Aström and T. Hägglund. *PID Controllers: Theory, Design, and Tuning*. 2nd ed. Instrument Society of America, 1995. URL: https://aiecp.wordpress.com/wp-content/uploads/2012/07/1-0-1-k-j-astrom-pid-controllers-theory-design-and-tuning-2ed.pdf.

[2] Ran Chen et al. "Stochastic optimization of levitation control system for maglev vehicles subjected to random guideway irregularity". In: *Journal of Sound and Vibration* 594 (Jan. 2025). ISSN: 10958568. DOI: 10.1016/j.jsv.2024.118682.

[3] J.P. Den Hartog. *Mechanical Vibrations*. Third edition. New York and London, 1947, pp. 366–375. URL: https://mheijd.home.xs4all.nl/Vibrations/Den%20Hartog%20-%20Mechanical%20vibrations.pdf.

[4] G G Denisov, E K Kugusheva and V V Novikov. *ON THE PROBLEM OF THE STABILITY OF ORE-DINENSIONAL UNBOUNDED ELASTIC SYSTEMS**. Tech. rep. 4. 1985, pp. 533–537.

[5] European Commission. *2050 long-term strategy - European Commission*. URL: https://climate.ec.europa.eu/eu-action/climate-strategies-targets/2050-long-term-strategy_en.

[6] Andrei B Faragau et al. *The interplay between the electro-magnetic and wave-induced instability mechanisms in the Hyperloop transportation system*. Tech. rep. Delft: Technical University of Delft, May 2024, pp. 617–627. URL: https://link.springer.com/chapter/10.1007/978-3-031-50631-4_52.

[7] Konstantinos Gkoumas. *Hyperloop academic research: A systematic review and a taxonomy of issues*. July 2021. DOI: 10.3390/app11135951.

[8] Hardt. *Hardt Hyperloop*. URL: https://docs.hardt.global/what-is-hyperloop/hyperloop-system-description.

[9] Guang He, Jie Li and Peng Cui. "Decoupling control design for the module suspension control system in maglev train". In: *Mathematical Problems in Engineering* 2015 (Jan. 2015). ISSN: 15635147. DOI: 10.1155/2015/865650.

[10] Junxiong Hu et al. "Levitation Stability and Hopf Bifurcation of EMS Maglev Trains". In: *Mathematical Problems in Engineering* 2020 (2020). ISSN: 15635147. DOI: 10.1155/2020/2936838. URL: https://www.researchgate.net/publication/340495097_Levitation_Stability_and_Hopf_Bifurcation_of_EMS_Maglev_Trains.

[11] Tsuyoshi Inoue and Yukio Ishida. "Nonlinear forced oscillation in a magnetically levitated system: The effect of the time delay of the electromagnetic force". In: *Nonlinear Dynamics* 52.1-2 (Apr. 2008), pp. 103–113. ISSN: 0924090X. DOI: 10.1007/s11071-007-9263-9.

[12] *ITF Transport Outlook 2019*. URL: https://www.oecd-ilibrary.org/sites/c013afc7-en/index.html?itemId=/content/component/c013afc7-en.

[13] James Stewart. *Calculus*. 8E. Toronto: Cenage Learning, 2017, p. 760.

[14] D. W. (Dominic William) Jordan and Peter Smith. *Nonlinear ordinary differential equations : an introduction for scientists and engineers*. Oxford University Press, 2007. ISBN: 9780199208241.

[15] Roman Lewandowski. "Nonlinear steady state vibrations of beams made of the fractional Zener material using an exponential version of the harmonic balance method". In: *Meccanica* 57.9 (Sept. 2022), pp. 2337–2354. ISSN: 15729648. DOI: 10.1007/s11012-022-01576-8.

[16] Canchang Liu et al. "Vibration control of disturbance gap for maglev vehicle considering stiffness change under unsteady aerodynamic forces". In: *Nonlinear Dynamics* 111.5 (Mar. 2023), pp. 4267–4282. ISSN: 1573269X. DOI: 10.1007/s11071-022-08054-6.

[17] T Mazilu. "Instability of a train of oscillators moving along a beam on a viscoelastic foundation". In: *Journal of Sound and Vibration* 332.19 (Sept. 2013), pp. 4597–4619. ISSN: 0022460X. DOI: 10.1016/j.jsv.2013.03.022.

[18] T Mazilu, M Dumitriu and C Tudorache. “On the dynamics of interaction between a moving mass and an infinite one-dimensional elastic structure at the stability limit”. In: *Journal of Sound and Vibration* 330.15 (July 2011), pp. 3729–3743. ISSN: 0022460X. DOI: 10.1016/j.jsv.2011.02.026.

[19] A V Metrikine and H A Dieterman. *Instability of vibrations of a mass moving uniformly along an axially compressed beam on a viscoelastic foundation*. Tech. rep. 5. 1997, pp. 567–576. URL: https://www.sciencedirect.com/science/article/pii/S0022460X9690783X.

[20] A. V. Metrikine. “Parametric instability of a moving particle on a periodically supported infinitely long string”. In: *Journal of Applied Mechanics, Transactions ASME* 75.1 (Jan. 2008), pp. 0110061–0110068. ISSN: 00218936. DOI: 10.1115/1.2745368.

[21] A. V. Metrikine. *Unstable lateral oscillations of an object moving uniformly along an elastic guide as a result of an anomalous Doppler effect*. Tech. rep. Mar. 1993. URL: https://www.researchgate.net/publication/252144882.

[22] Lambros Mitropoulos et al. *The hyperloop system and stakeholders: A review and future directions*. July 2021. DOI: 10.3390/su13158430. URL: https://www.mdpi.com/2071-1050/13/15/8430.

[23] Pedro Museros et al. “Key aspects in the analysis and design of Hyperloop™ infrastructure under static, dynamic and thermal loads”. In: *Engineering Structures* 239 (July 2021). ISSN: 18737323. DOI: 10.1016/j.engstruct.2021.112177.

[24] Ali Hassan Nayfeh and Dean Mook. “Nonlinear Oscillations”. In: (Jan. 1979). URL: https://edisciplinas.usp.br/pluginfile.php/5182350/mod_resource/content/1/Nonlinear%20Oscillations.pdf.

[25] Jonas Kristiansen Noland. “Prospects and Challenges of the Hyperloop Transportation System: A Systematic Technology Review”. In: *IEEE Access* 9 (2021), pp. 28439–28458. ISSN: 21693536. DOI: 10.1109/ACCESS.2021.3057788.

[26] Jin Woo Park et al. “Controller design with high fidelity model for a passive maglev tray system”. In: *International Journal of Precision Engineering and Manufacturing* 15.8 (2014), pp. 1521–1528. ISSN: 20054602. DOI: 10.1007/s12541-014-0500-0.

[27] Jithu Paul et al. “Suppression of parametric resonance using a state-dependent parametric force: A Hyperloop case study”. In: ().

[28] Rajendra K. Praharaj and Nabanita Datta. “Dynamic response of Euler–Bernoulli beam resting on fractionally damped viscoelastic foundation subjected to a moving point load”. In: *Proceedings of the Institution of Mechanical Engineers, Part C: Journal of Mechanical Engineering Science* 234.24 (Dec. 2020), pp. 4801–4812. ISSN: 20412983. DOI: 10.1177/0954406220932597.

[29] Seaworld. *Adaptations*. 2024. URL: https://seaworld.org/animals/all-about/bottlenose-dolphin/adaptations/.

[30] J M J Spijkers, A W C M Vrouwenvelder and E C Klaver. *Structural Dynamics CT 4140 Part 1-Structural Vibrations*. Tech. rep. 2005.

[31] Steven H. Strogatz. *NONLINEAR DYNAMICS AND CHAOS*. Second edition. CRC Press, 2015. URL: https://www.biodyn.ro/course/literatura/Nonlinear_Dynamics_and_Chaos_2018_Steven_H._Strogatz.pdf.

[32] Yougang Sun et al. “Dynamic analysis and vibration control for a maglev vehicle-guideway coupling system with experimental verification”. In: *Mechanical Systems and Signal Processing* 188 (Apr. 2023). ISSN: 10961216. DOI: 10.1016/j.ymssp.2022.109954.

[33] United Nations. *Population | United Nations*. URL: https://www.un.org/en/global-issues/population.

[34] Meiqi Wang et al. “Parameter optimization of electromagnetic suspension-type maglev train control system based on multi-objective grey wolf non-dominated sorting hybrid algorithm-□ hybrid algorithm”. In: *Journal of Low Frequency Noise Vibration and Active Control* 43.2 (June 2024), pp. 956–978. ISSN: 20484046. DOI: 10.1177/14613484231214915.

[35] A.R.M. Wolfert. “WAVE EFFECTS IN ONE-DIMENSIONAL ELASTIC SYSTEMS INTERACTING WITH MOVING OBJECTS”. In: (Mar. 1999). URL: https://repository.tudelft.nl/islandora/object/uuid%3A32cb2d0d-0660-4356-b286-18ecc4c947ed.

[36] Han Wu, Xiao Hui Zeng and Yang Yu. “Motion stability of high-speed maglev systems in consideration of aerodynamic effects: a study of a single magnetic suspension system”. In: *Acta Mechanica Sinica/Lixue Xuebao* 33.6 (Dec. 2017), pp. 1084–1094. ISSN: 16143116. DOI: 10.1007/s10409-017-0698-z.

[37] Han Wu et al. “Dynamic stability of an electromagnetic suspension maglev vehicle under steady aerodynamic load”. In: *Applied Mathematical Modelling* 97 (Sept. 2021), pp. 483–500. ISSN: 0307904X. DOI: 10.1016/j.apm.2021.04.008.

[38] Junqi Xu and Yuan Zhou. “A nonlinear control method for the electromagnetic suspension system of the maglev train”. In: *Journal of Modern Transportation* 19.3 (2011), pp. 176–180. DOI: 10.3969/j.issn.2095-087X.2011.03.005.

[39] Junqi Xu et al. “Nonlinear dynamic analysis on maglev train system with flexible guideway and double time-delay feedback control”. In: *Journal of Vibroengineering* 19.8 (Dec. 2017), pp. 6346–6362. ISSN: 13928716. DOI: 10.21595/jve.2017.18970.

[40] J. D. Yau. “Aerodynamic vibrations of a maglev vehicle running on flexible guideways under oncoming wind actions”. In: *Journal of Sound and Vibration* 329.10 (2010), pp. 1743–1759. ISSN: 10958568. DOI: 10.1016/j.jsv.2009.11.039.

A

Appendix A

The stability planes are illustrated for wavelengths of 20 m, 80 m, and 120 m for the irregular Euler-Bernoulli beam with continuous support under an electromagnetically suspended moving mass. These stability planes show how the stability boundaries change for various velocities and wavelengths.

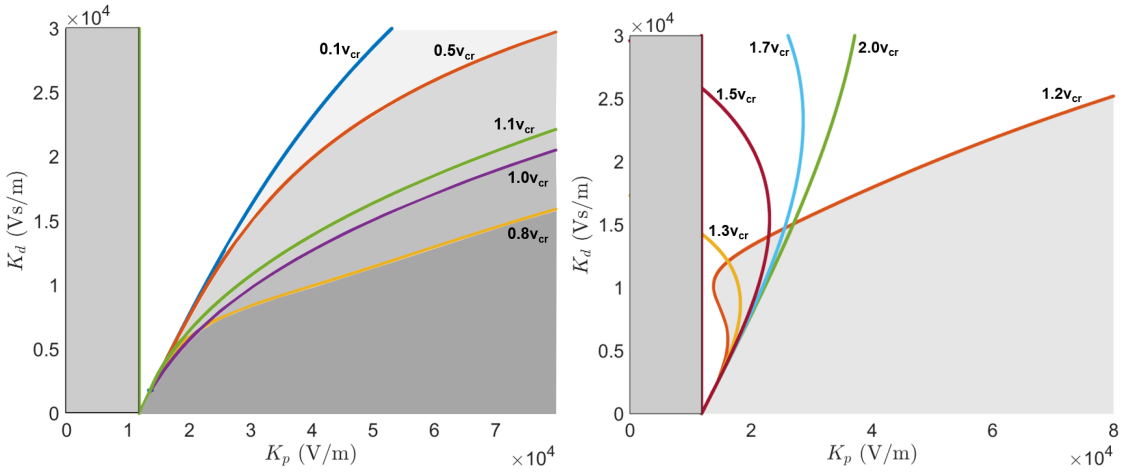

(a) $v = 0.1 - 1.1v_{cr}$ m/s, and $L = 20$ m

(b) $v = 1.2 - 2.0v_{cr}$ m/s, and $L = 20$ m

Figure A.1: Stability planes for varying velocities and a constant wavelength of the surface roughness

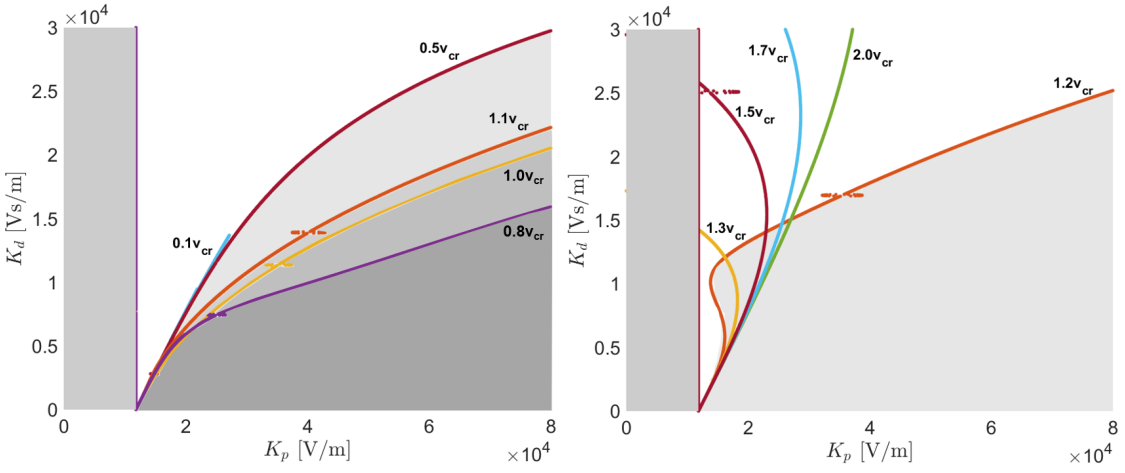

(a) $v = 0.1 - 1.1v_{cr}$ m/s, and $L = 80$ m

(b) $v = 1.2 - 2.0v_{cr}$ m/s, and $L = 80$ m

Figure A.2: Stability planes for varying velocities and a constant wavelength of the surface roughness

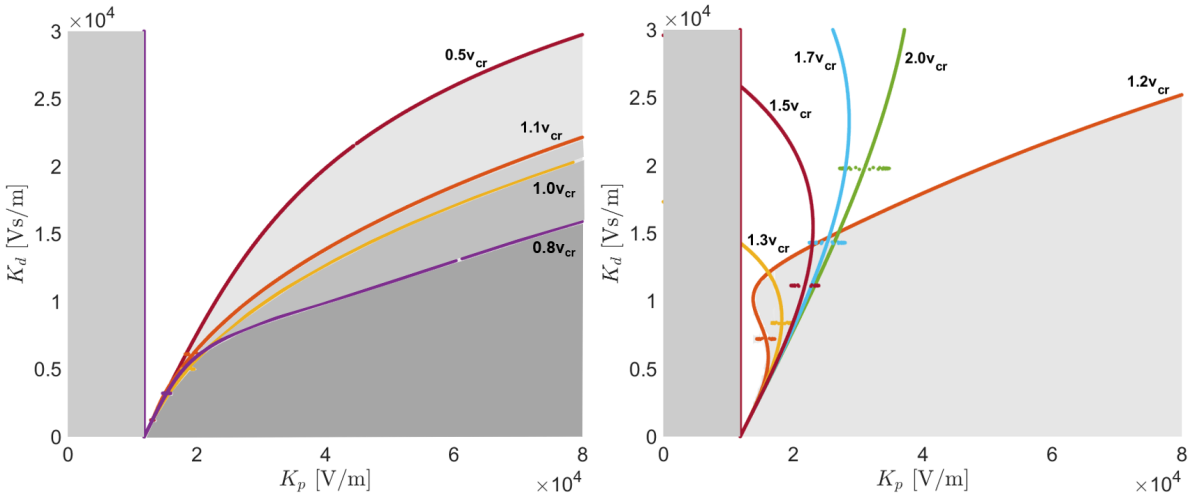

(a) $v = 0.1 - 1.1v_{cr}$ m/s, and $L = 120$ m

(b) $v = 1.2 - 2.0v_{cr}$ m/s, and $L = 120$ m

Figure A.3: Stability planes for varying velocities and a constant wavelength of the surface roughness

B

Appendix B

The previous figures show that the ellipses, which represent parametric resonance, shift as the wavelength of the irregularity changes. In this section, the wavelength is varied systematically to understand the relation between the wavelength and the region of parametric resonance, and whether the varying wavelength influences other aspects of the stability boundary.

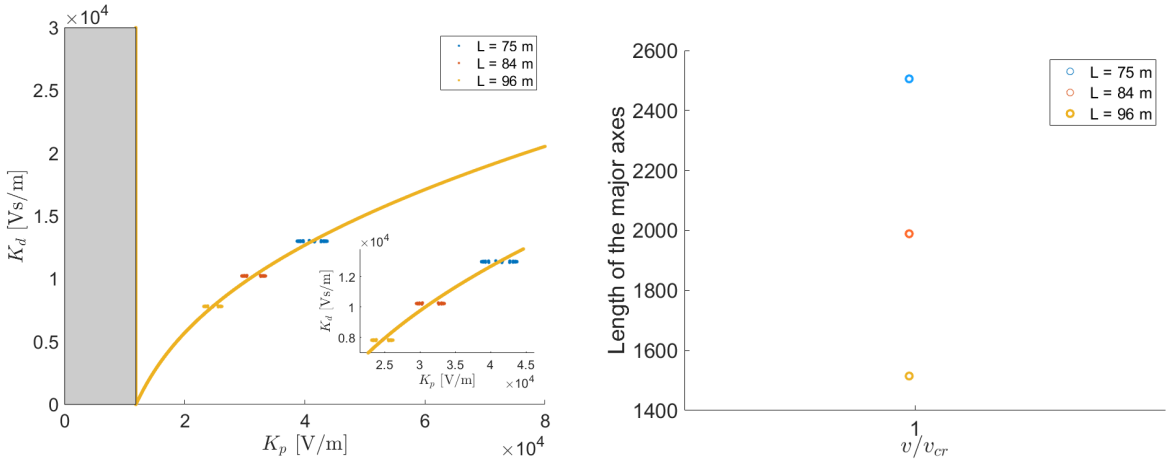

(a) Stability plane for various wavelengths

(b) Length of the major axes for a varying wavelength

Figure B.1: Stability planes for different surface roughness wavelength at $v = 1.0v_{cr}$ m/s

The results are also compared to the 1.5 DOF system, where the excitation frequencies are changed to match those of the irregular guideway profile. This comparison gives insights into the accuracy of the 1.5 DOF system and the influence of the beam dynamics on the stability of the system.

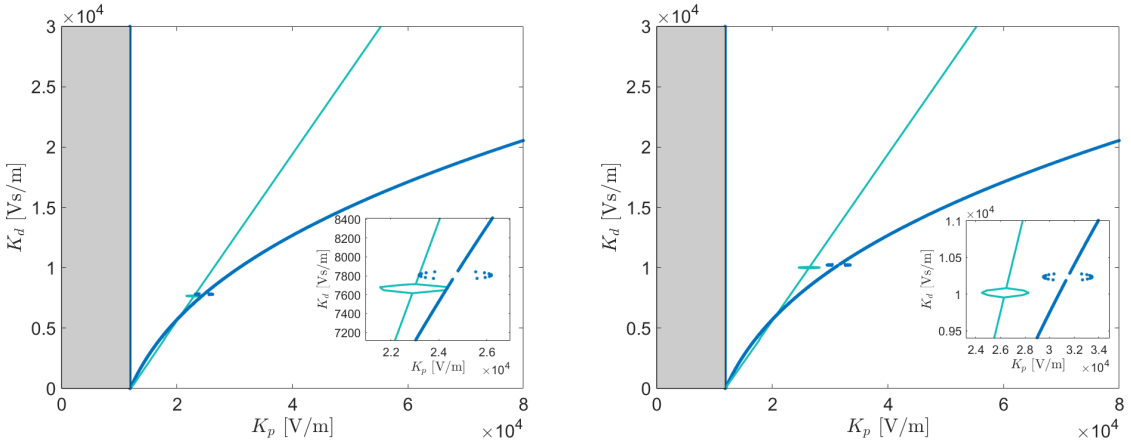

(a) $\omega_1 = 70$ rad/s and $L = 96$ m

(b) $\omega_1 = 80$ rad/s and $L = 84$ m

Figure B.2: Stability planes for varying surface roughness wavelength at $v = 1.0v_{cr}$ m/s

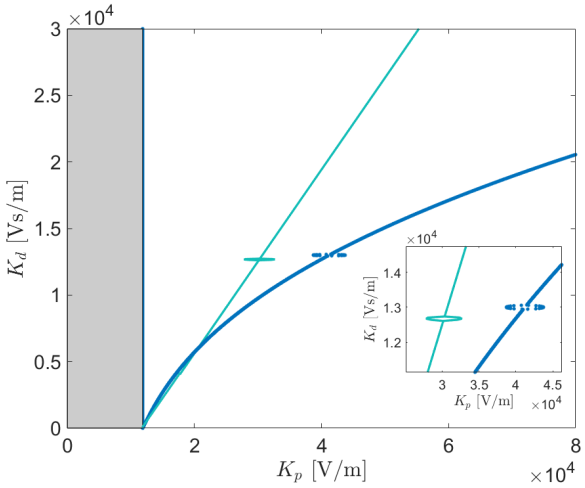

Figure B.3: Stability planes for varying surface roughness wavelength at $v = 1.0v_{cr}$ m/s, $\omega_1 = 90$ rad/s and $L = 75$ m

C

Appendix C

These stability planes illustrate the comparison between the irregular Euler-Bernoulli beam with continuous support under an electromagnetically suspended moving mass and the 1.5 DOF electromagnetically suspended mass. In this comparison, the excitation frequency from the irregular guideway profile matches that of the oscillating base.

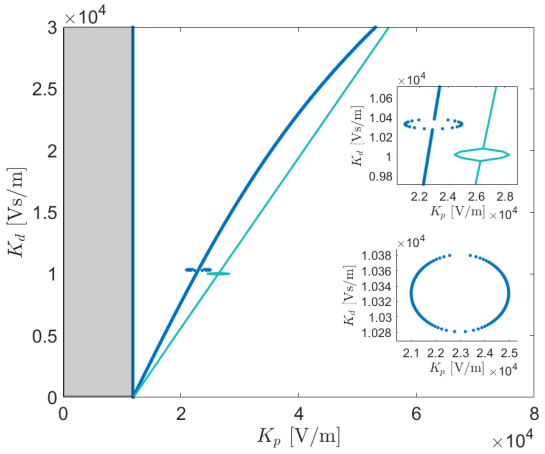

(a) $v = 0.1v_{cr}$, $L = 8.4$ m, and $\omega_1 = 80$ rad/s

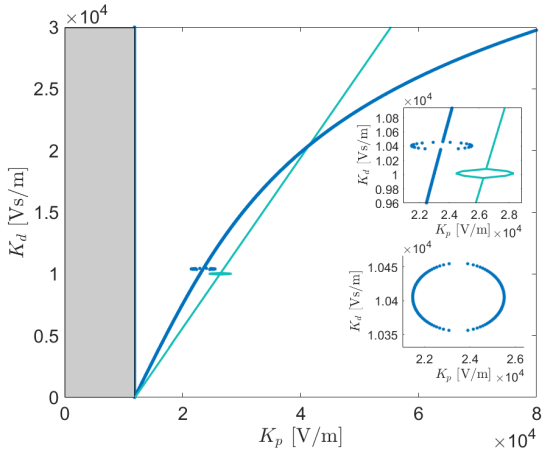

(b) $v = 0.5v_{cr}$, $L = 42.1$ m, and $\omega_1 = 80$ rad/s

Figure C.1: Stability planes with an excitation frequency maintained at 80 rad/s by changing the surface roughness wavelength

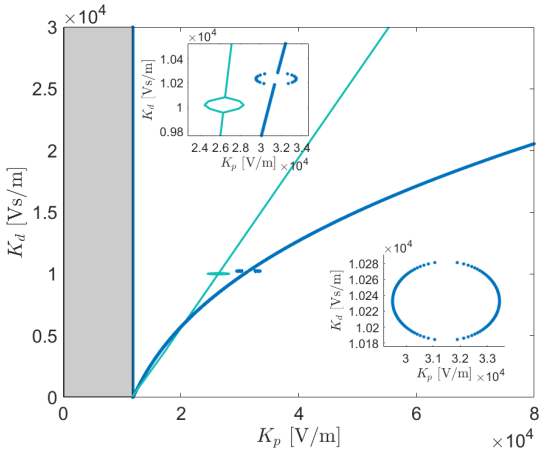

(a) $v = 1.0v_{cr}$, $L = 84.3$ m, and $\omega_1 = 80$ rad/s

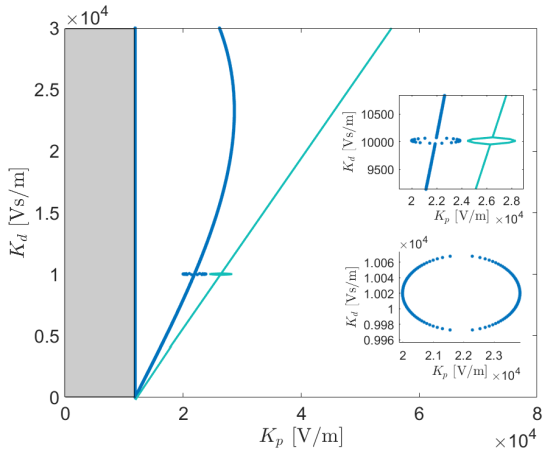

(b) $v = 1.7v_{cr}$, $L = 143.3$ m, and $\omega_1 = 80$ rad/s

Figure C.2: Stability planes with an excitation frequency maintained at 80 rad/s by changing the surface roughness wavelength